

## Accepted Manuscript

Full length article

Bioengineered tumoral microtissues recapitulate desmoplastic reaction of pancreatic cancer

Virginia Brancato, Valentina Comunanza, Giorgia Imparato, Davide Corà, Francesco Urciuolo, Alessio Noghero, Federico Bussolino, Paolo A. Netti

PII: S1742-7061(16)30668-7

DOI: <http://dx.doi.org/10.1016/j.actbio.2016.11.072>

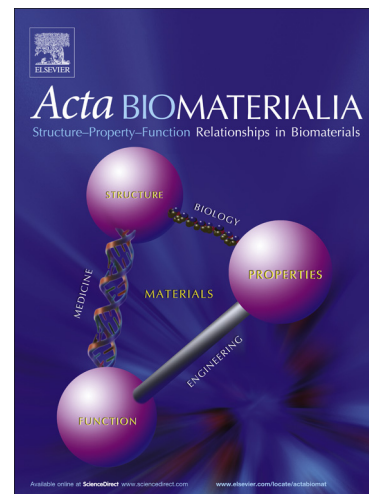
Reference: ACTBIO 4581

To appear in: *Acta Biomaterialia*

Received Date: 15 July 2016

Revised Date: 7 November 2016

Accepted Date: 30 November 2016



Please cite this article as: Brancato, V., Comunanza, V., Imparato, G., Corà, D., Urciuolo, F., Noghero, A., Bussolino, F., Netti, P.A., Bioengineered tumoral microtissues recapitulate desmoplastic reaction of pancreatic cancer, *Acta Biomaterialia* (2016), doi: <http://dx.doi.org/10.1016/j.actbio.2016.11.072>

This is a PDF file of an unedited manuscript that has been accepted for publication. As a service to our customers we are providing this early version of the manuscript. The manuscript will undergo copyediting, typesetting, and review of the resulting proof before it is published in its final form. Please note that during the production process errors may be discovered which could affect the content, and all legal disclaimers that apply to the journal pertain.

## Bioengineered tumoral microtissues recapitulate desmoplastic reaction of pancreatic cancer

Virginia Brancato<sup>1a</sup>, Valentina Comunanza<sup>2,3,a</sup>, Giorgia Imperato<sup>4\*</sup>, Davide Corà<sup>2,3</sup>, Francesco Urciuolo<sup>4</sup>, Alessio Noghero<sup>2,3</sup>, Federico Bussolino<sup>2,3</sup> and Paolo A. Netti<sup>\*1,4,5</sup>

<sup>1</sup> Interdisciplinary Research Centre on Biomaterials (CRIB), University of Naples Federico II P.le Tecchio 80, Naples, Italy

<sup>2</sup> Department of Oncology. University of Torino - SP 142 km 3.95, 10060 Candiolo, Italy

<sup>3</sup> Candiolo Cancer Institute – IRCCS – SP 142 km 3.95, 10060 Candiolo, Italy

<sup>4</sup> Center for Advanced Biomaterials for HealthCare@CRIB, Istituto Italiano di Tecnologia, Largo Barsanti e Matteucci 53, 80125 Naples, Italy

<sup>5</sup> Department of Chemical, Materials and Industrial Production (DICMAPI) University of Naples Federico II, P.le Tecchio 80; Naples, Italy

<sup>a</sup>these two authors contributed equally to this work

\*Corresponding Author

Giorgia Imperato

Center for Advanced Biomaterials for HealthCare@CRIB Istituto Italiano di Tecnologia, Largo Barsanti e Matteucci n. 53, 80125 Naples, Italy

Telephone: +39 081 19933100

Fax: +39 081 19933140

e-mail: giorgia.imparato@iit.it

**Abstract**

Many of the existing three-dimensional (3D) cancer models *in vitro* fail to represent the entire complex tumor microenvironment composed of cells and extra cellular matrix (ECM) and do not allow a reliable study of the tumoral features and progression. In this paper we reported a strategy to produce 3D *in vitro* microtissues of pancreatic ductal adenocarcinoma (PDAC) for studying the desmoplastic reaction activated by the stroma-cancer crosstalk. Human PDAC microtissues were obtained by co-culturing pancreatic cancer cells (PT45) and normal or cancer-associated fibroblasts within biodegradable microcarriers in a spinner flask bioreactor. Morphological and histological analyses highlighted that the presence of fibroblasts resulted in the deposition of a stromal matrix rich in collagen leading to the formation of tumor microtissues composed of a heterotypic cell population embedded in their own ECM. We analyzed the modulation of expression of ECM genes and proteins and found that when fibroblasts were co-cultured with PT45, they acquired a myofibroblast phenotype and expressed the desmoplastic reaction markers. This PDAC microtissue, closely recapitulating key PDAC microenvironment characteristics, provides a valuable tool to elucidate the complex stroma–cancer interrelationship and could be used in a future perspective as a testing platform for anticancer drugs in Tissue-on-chip technology.

**Keywords**

Tumor in vitro, 3D microtissue, stroma, tumor microenvironment, desmoplasia, pancreatic cancer

## 1. Introduction

Cells in their natural environment grow within an organized 3D matrix, which deeply influences physiological and pathological events occurring in the tissue. Tumors are often studied *in vitro* by means of extremely simplified 2D cell cultures or expensive and ethically problematic animal model systems [1,2]. The latter may not adequately reproduce some features of human tumors, in particular therapeutic responses and mechanisms sustaining drug resistance [3,4]. In this scenario 3D tissue-engineered tumor models are emerging as the most promising tool to investigate *in vitro* tumor formation and evolution, as well as stroma-tumor cross-talk in order to identify new genetic drivers and therapeutic targets [5-12]. The most widely used 3D biomimetic cancer models are spheroids, because of their 3D architecture. They cannot, however, recapitulate all features of solid tumors, since they lack the interactions with the ECM that plays a key-role in tumor progression and chemoresistance [13]. To overcome such limitations, many groups tried to incorporate a cancer-stromal cell mix (usually fibroblasts) into a 3D matrix, such as matrigel or collagen type I, to recreate the complex tissue architecture seen *in vivo*. In our understanding, they only provide an exogenous matrix in which the tumor cells are not enabled to establish the physiological cell-cell and cell-ECM interactions normally experienced *in vivo*. Moreover, these scaffolds often suffer from batch-to-batch variations and their performance is impaired by an incomplete understanding of their impact on cell behavior [4, 14-16]. PDAC is one of the most aggressive cancers and is the fourth leading cause of cancer death worldwide. It is specifically characterized by a desmoplastic reaction, a process in which fibrous tissue infiltrates into and envelops the cellular compartments, including cancer and stroma cells (endothelial cells, immune and endocrine cells, fibroblasts and stellate cells) [17-20]. Desmoplastic reaction is associated with accelerate proliferation of myofibroblasts, differentiated cells deriving from mesenchymal or stellate cells [21,22] and it is characterized by the up-regulation of matricellular components such as versican, periostin, fibronectin and hyaluronic acid [21,23]. Moreover, the invasiveness of PDAC is due to the continue cross-talk between fibroblasts and cancer cells [24]. Tumor cells drive differentiation of fibroblasts or mesenchymal stem cells into highly contractile and matrix-depositing myofibroblasts, expressing  $\alpha$ -SMA, Vimentin and PDGFR $\beta$ , thereby promoting enhanced ECM assembly, alignment, unfolding, and cross-linking of collagen type I- and fibronectin-rich matrices [2]. Furthermore, the aberrant fibrotic reaction compresses vessels thus limiting perfusion with consequent poor drug delivery [25,26]. The complexity of the pancreatic tumor microenvironment makes hard to study the development of this form of cancer; in particular, little is known about the mechanism involving pancreatic cancer cells and stroma [27]. Since recent studies have reported that the direct physical contact between stromal and cancer cells better represent the *in vivo* microenvironment [28], there



is an urgent need of realistic models able to recapitulate such a situation *in vitro*. In our survey we adapted already established tissue engineering strategies to obtain dermal microtissues to the need of producing pathological microunits [29]. We succeeded in fabricating a novel 3D *in vitro* microtissue of human PDAC by co-culturing PT45 cell line carrying mutated *KRAS* [30-33] and human normal or cancer-associated fibroblasts within biodegradable gelatin microcarriers in a spinner flask bioreactor. First, we produced homotypic culture of normal and tumoral stroma microtissues and assessed the difference in terms of gene expression, matrix deposition and cell growth between the two models. Then we investigated the interaction between stroma and pancreatic cancer cells analyzing ECM proteins and the genes modulated between homotypic and heterotypic models. The produced PDAC microtissues resulted in a complex biological system in which cells were embedded in their own ECM experiencing physiological cell-cell and cell-ECM interactions. These features strongly distinguish the proposed model from a mere 3D cell aggregate highlighting new insights in the fundamental regulatory role of the ECM in tumor progression. At last, these tumor microtissues could provide a new tool for the characterization of disease progression and drug resistance mechanisms *in vitro*. Moreover due to their size at a millimetric scale, they could be easily inserted in microfluidic devices for tissue-on-chip applications [34].

## 2. Materials and Methods

### 2.1 3D tumor microtissue formation

#### 2.1.1 Microscaffold production

Gelatin porous microbeads (GPMs) were prepared according to a modified double emulsion protocol (O/W/O) [35]. GPMs were stabilized by crosslink reaction with GPMs glycerinaldehyde (GAL), in order to make them stable in aqueous environment at 37 °C, finally they were sterilized in absolute ethanol and washed in PBS as previously described [29].

Briefly, Gelatin porous microbeads (GPMs) have been prepared according to a modified double emulsion technique (O/W/O). Gelatin (type B Sigma Aldrich Chemical Company, Bloom 225, Mw¼176,654 Da) was dissolved into 10 ml of water containing TWEEN 85 (6% w/v) (Sigma Aldrich Chemical Company). The solution was kept at 40°C. Toluene containing SPAN 85 (3% w/v) (Sigma Aldrich Chemical Company) was continuously added to the aqueous gelatin solution (8% w/v) to obtain primary oil in water emulsion. The added toluene formed droplets in the gelatin solution until saturation. Beads of gelatin containing droplets of toluene were produced through the addition of excess toluene (30 ml) that allowed for a double emulsion (O/W/O). After cooling below 5°C, 20 ml of ethanol were added to extract toluene and stabilize GPMs. The resulting microspheres were filtered and washed with acetone and then dried at room temperature. Microspheres were separated selectively by using commercial sieves (Sieves IG/3-EXP, Retsch,

Germany). GPMs with 75  $\div$  150  $\mu\text{m}$  size range were recovered and further processed. GPMs have been stabilized by means of chemical treatment with 5% glyceraldehyde (GAL), in order to make them stable in aqueous environment at body temperature. In particular, GPMs were dispersed into an acetone/water solution containing different amounts of GAL and mixed at 4°C for 24 h. Then microspheres were filtered and washed with acetone and dried at room temperature. GPMs have spherical shape, the mean internal pore size is 10–20  $\mu\text{m}$  and histological sections [29] of microtissues show that pore are well interconnected to allow the seeding and spreading of the cells throughout the scaffold.

### 2.1.2 Cell-type

Human normal fibroblasts (NF) and cancer associated fibroblast (CAF), kindly donated by Kojima's group [36], were cultivated in high glucose DMEM with GlutaMAX (ThermoFisher), supplemented with 10% heat inactivated and fetal bovine serum, and 100 U/ml penicillin/streptomycin. PDAC cells (PT45) [29-32] were kindly donated by Dr. P. Allavena (Humanitas, Milano, I) and sub-cultured in RPMI-1640 medium (Sigma) supplemented with 10% heat inactivated fetal bovine serum, 100  $\mu\text{g}/\text{ml}$  L-glutamine, 100 U/ml penicillin/streptomycin. Cells were maintained at 37 °C in humidified atmosphere containing 5% CO<sub>2</sub>. For 2D co-cultures experiments cells were mixed in suspension 1:3 (PT45/NF or PT45/CAF) ratio and plated at a density of 3000 cell/cm<sup>2</sup>.

### 2.1.3 Lentivirus production and cell infection

Virus was produced in HEK-293T cells calcium phosphate transfected (kit Promega) with pLVX-DsRed-Express2-N1 or pLVX-ZsGreen1-N1 vectors (Clontech, USA). Supernatant was collected at 48 and 72 h post transfection and filtered through a 0.4- $\mu\text{m}$  Nalgene filtration unit. Lentiviral particles supernatants were concentrated by ultracentrifugation at 19.500 g for 2 h at 20 °C. The viral titer was determined by transducing Hela cells with serial dilutions of virus. Stromal NF and CAF cells were infected with pLVX-DsRed-Express2-N1 (Red) while PT45 tumor cells with pLVX-ZsGreen1-N1 (Green). Selection was achieved by a 24 h incubation with puromycin (2  $\mu\text{g}/\text{ml}$ ).

### 2.1.4 Homotypic cell culture

All cell cultures on microscaffolds were performed in a spinner flask (100 ml Cellspin, Integra) by following a previously established procedure [29]. For the homotypic culture (NF, CAF and PT45 alone) 50 mg of GPMs were loaded together with  $7.5 \times 10^5$  cells (30cell/GMP ratio). To promote cell seeding on GMPs an intermittent stirring regime (30 min at 0 rpm, 5 min at 30 rpm) for 6 h was performed. To monitor the seeding efficiency during the post-inoculum time, the disappearance of

free cells from the inoculated spinner cultures was calculated as  $[(C_0 - C_t) * 100] / C_0$  where  $C_0$  is the concentration of the cells at the inoculum time and  $C_t$  the concentration of the cells in the culture medium. Then, dynamic cultures were kept under continuous stirring at 30 rpm for up to 12 d. Medium was changed on the first day and every 3 days until the end of the experiments. From the second day of dynamic culture, 50  $\mu\text{g/ml}$  of ascorbic acid were added. Microtissues ( $\mu\text{TP}$ ) samples were taken for further investigations at days 1, 4, 8 and 12 for homotypic cultures and fixed. At the same days of culture, 1 ml aliquots were collected for cell growth monitoring on the GPM. Briefly, 200  $\mu\text{l}$  of the same aliquots were transferred to a cell culture dish (w/2 mm grid Nunc) for microcarrier counting, after which the microcarrier suspension was placed in a new 2 ml tube and washed twice with PBS. To detach cells from microcarriers,  $\mu\text{TP}$  were digested by collagenase A (Roche Life sciences, Italy) 60 min at 37 °C, centrifuged 5 min at 2000 rpm and incubated 5 min in Trypsin (Lonza, Italy). The detached cells were then counted using a hemocytometer. Over the entire dynamic cell culture period in spinner flask, 500  $\mu\text{l}$  aliquots were collected at days 1, 4, 8 and 12 for cell distribution monitoring during  $\mu\text{TP}$  assembling. Confocal Leica TCS SP5 II combined with a Multiphoton Microscope where the NIR femtosecond laser beam was derived from a tunable compact mode-locked titanium:sapphire laser (Chameleon Compact OPO-Vis, Coherent) was used. All the cells were stable transfected so they were monitored “live” without fixing procedure, on the day of the experiment.

### **2.1.5 Heterotypic cell culture**

For heterotypic cultures, PT45 were added in the spinner flask at day 6 of the homotypic culture of NF or CAF (Fig.1). According to previous works [37,38] and supported by pilot experiments in which we tried various cancer cell/fibroblasts ratio (1:1; 1:2 and 1:3, data not shown), we found that the 1:3 ratio was the most suitable for our purpose because it allows fibroblasts to grow and produced ECM. The number of PT45 was stabilized in order to guarantee a ratio of PT45 to stromal cells equal to 1:3.  $\mu\text{TP}$  samples were taken for assay at days 1, 4, 6, 7 and 12 for heterotypic cultures. Cell counting was performed at day 1, 4, 6 (when pancreatic cells were added), 7 and 12 for heterotypic cultures. For co-cultures, samples were observed at day 4, 6, 7, and 12 at confocal microscope to monitor  $\mu\text{TP}$  morphology.

## **2.2 Tumor microtissue characterization**

### **2.2.1 Gelatin zymography**

Gelatin zymography was performed for both NF- $\mu\text{TP}$  and CAF- $\mu\text{TP}$  culture supernatants as follows: gel (SDS-PAGE, 10%) was copolymerized with gelatin (0.1%) (Sigma-Aldrich). Electrophoresis was carried out using the minigel lab apparatus Mini Protean 3 (Biorad) at a constant voltage of 150 V until the dye reached the bottom of the gel. Following electrophoresis, gel was washed in

renaturation buffer (2.5% Triton X-100 in 50 mM Tris-HCl, pH 7.5) for 1 h in an orbital shaker. Then the gel was incubated for 18 h at 37 °C in incubation buffer (0.15 M NaCl, 10 mM CaCl<sub>2</sub>, 0.02% NaN<sub>3</sub> in 50 mM Tris-HCl pH 7.5). Gel was then stained with Coomassie blue and destained with 30% methanol and 10% acetic acid. Areas of enzymatic activity appeared as clear bands over the dark background. Following zymography, the degree of gelatin digestion was quantified using Image J software and the image was digitally inverted, so that the integration of bands was reported as positive values. We reported the pixel intensity of the area of each gelatin-digested band.

### 2.2.2 Areas analysis

For area analysis, 1 ml of  $\mu$ TP homotypic culture at day 4, 8 and 12 on a 35 mm Petri dish were observed with a light microscope (Olympus, BX53). Twenty images were taken at the same magnification for each sample at every time-point. Area was calculated using Image J software. Briefly, scanned color image was converted to an 8-bit grayscale format; hence, measurement scale was set and automated threshold included only dark areas. At last, particles were analyzed and the area was calculated.

### 2.2.3 Collagen fraction and GLCM texture analysis

Two-photon excited fluorescence was used to induce second harmonic generation (SHG) and obtain high-resolution images of unstained collagen structures in  $\mu$ TP's ECM. Hence, the samples were observed exploiting the different fluorescence from the lentiviral vector used as described before (pLVX -DsRed-express2-N1 with  $\lambda_{ex}=554\text{nm}$ ,  $\lambda_{em}=591\text{nm}$ ; pLVX-ZsGreen1-N1  $\lambda_{ex}=493\text{nm}$ ,  $\lambda_{em}=505\text{nm}$ ) as well as to induce second harmonic generation (SHG) ( $\lambda=840\text{ nm}$ ). Homotypic and heterotypic  $\mu$ TP samples were used for SHG analysis by using ImageJ<sup>®</sup> software. In order to quantify the collagen fraction in the endogenous ECM, the ROI were chosen by excluding the signal rising from the microbeads. The collagen portion in the ECM space was represented by the bright pixels ( $N_c$ ) in grayscale rising from the SHG signal, while the non-collagen portion appeared as black pixels ( $N_b$ ). We define collagen fraction (CF) as the ratio between bright pixels to total pixels in the selected ROI. We also correlated this ratio to the cell number in the ROI, counting the nuclei [39]. Moreover, to quantitatively assess the collagen-related changes in the architecture we performed Grey-Level Co-occurrence Matrix (GLCM) texture analysis, using the ImageJ plug-in "Texture" on SHG images, according to the procedure previously described [40].

### 2.2.4 Histological and immunohistochemical analysis

One ml of  $\mu$ TP suspension was formalin-fixed and paraffin embedded. Successively, the samples were sectioned at a thickness of 7  $\mu\text{m}$ . Masson's trichrome (Sigma Aldrich) and Alcian Blue (Bioptica) stainings were performed according to standard protocols. At last, the sections were mounted with Histomount Mounting Solution (Bioptica) on coverslips and the morphological

features of  $\mu$ TP were observed with a light microscope (Olympus, BX53). The images obtained were processed by means of ImageJ<sup>®</sup> software. For Masson's trichrome and Alcian Blue staining, we consider the Blue staining, indicative of ECM and glycosaminoglycans deposition, that was separated from other colours by manual thresholding of hue (121-179), saturation (20-255), and brightness (10-255) values. Then, the ECM deposition was quantified as mean percentage of blue staining area. Ten sections were used and at least five different fields were randomly examined in each section for each time point. For immunohistochemical staining (IHC) of anti-human Ki-67,  $\alpha$ -SMA, Vimentin and PDGF $\beta$ -r (Abcam, UK). A mouse and rabbit specific HRP/DAB (ABC) detection kit (Abcam, UK) was used according to the manufacturer's protocol.

### **2.2.5 Immunofluorescence analysis**

Samples from 1 ml of  $\mu$ TP suspension were frozen in OCT compound and cut into 10- $\mu$ m thick sections after overnight treatment at 4 °C in a 30% sucrose solution. Tissue slices were fixed in 4% paraformaldehyde for 10 min at room temperature. The antibodies used for tissue immunofluorescence (IF) staining were as follows: anti- $\alpha$ -SMA (Sigma); anti-POSTN and anti-Versican (Abcam). The sections were then incubated with the appropriate fluorescence-conjugated secondary antibodies (Alexa 647 or 488, Life Technologies), and nuclei were counterstained with DAPI (Life Technologies). The samples were mounted using fluorescent mounting medium (Dako). All immunofluorescence images were captured and analyzed using a Leica SPEII confocal laser-scanning microscope (Leica Microsystems). Image acquisition was performed maintaining the same laser power, gain and offset settings. Multiple independent fields (10-15 for every sections; 40X magnification) were randomly chosen and analyzed. Image quantification was performed using NIH ImageJ and expressed as the percentage of the fluorescence area relative to the protein signal respect to the whole image's area.

## **2.3 Gene expression analysis**

### **2.3.1 Fluorescence-Activated Cell Sorting Analysis**

Single-cell suspensions of 3D co-culture  $\mu$ TP or corresponding 2D co-cultures were prepared as follows:  $\mu$ TP or cells were digested in StemPro Accutase (Thermofisher). Enzymatic digestion was incubated at 37 °C for 15-20 min prior to the substrate being passed through a 70- $\mu$ m cell strainer. The resulting cell suspension was washed and centrifuged at 1200 RPM for 5 min and re-suspended in MACS buffer with DAPI (Life Technologies). To exclude dead cells, DAPI was added immediately prior to sorting. The purity of DsRed<sup>+</sup> (NF and CAF) and ZsGreen<sup>+</sup> (PT45) cells was assessed by flow cytometry Cyan ADP Analyzer (Beckman Counter) and was above 90%. DsRed<sup>+</sup> (NF and CAF) and ZsGreen<sup>+</sup> (PT45) cells were sorted by fluorescence-activated cell sorting (FACS) using a MoFlo<sup>™</sup> XDP High-Performance Cell sorter (Beckman Coulter). Data were

acquired and analyzed using Summit v5.2 software (Beckman Coulter, Inc., Fullerton, CA, USA). The sorted cells were immediately stored in Qiazol Lysis reagent (Qiagen).

### **2.3.2 RNA extraction and quantitative Real Time PCR**

Total RNA was extracted from tumors using an RNeasy mini kit (Qiagen). For cDNA synthesis, a High Capacity cDNA Reverse Transcription kit (Life Technologies) was used according to the manufacturer's instructions. An RNA quality check, including concentration and purity, was performed with a Nanodrop ND-100 (Nanodrop Technologies). Quantitative real time PCR was performed on a CFX96 (Bio-Rad) using SYBR-green PCR MasterMix (Life Technologies). The PCR thermal profiles were 95 °C for 15 s and 60 °C for 60 s (40 cycles). All experiments were performed in triplicate. Melting curve analysis was performed for each PCR reaction to confirm the specificity of the amplifications. The housekeeping gene TBP was used to normalize the expression data. The primer sequences and product sizes are indicated in Table S1.

### **2.3.3 Microarray-based transcriptional profiling and bioinformatics analysis of microarray data**

For gene expression profiling analysis, 300 ng of total RNA was amplified and labeled using an Illumina TotalPrep RNA Amplification Kit (Life Technologies). A total of 750 ng cRNA probes was hybridized on the HumanHT-12 v4.0 Expression Bead Chip (Illumina). All experiments were performed in biological triplicate (duplicate for 2D groups). Cubic spline-normalized probe intensity data, together with detection p-values, were obtained using the GenomeStudio software V2011.01 (Illumina). We selected for further analysis probes characterized by at least one experimental point having a detection p-value < 0.05. For each gene, we retained the associated probe with the largest mean expression value across all samples. The data were then  $\log_2$  transformed for all subsequent analyses. For each probe, the  $\log_2$  signal in each sample was converted to the  $\log_2$  ratio against the global average expression of that probe in all samples. The  $\log_2$  ratio expression data were clustered and visualized using GEDAS software [41]. One-way ANOVA test and LIMMA [42] were used to identify the modulated genes. For the ANOVA test, p-values were corrected for multiple testing using a Benjamini–Hochberg procedure [43], and a cutoff of 0.1 for the false discovery rate (FDR) was used to define differentially modulated genes across all four experimental conditions. In the LIMMA analysis, a threshold of  $|\log_2 \text{FC}|$  of 1 and adjusted p-value < 0.1 were used to select differentially expressed genes; for each pair-wise comparison, each of the treatments was compared separately to the control samples. All the statistical analyses were performed within the R environment (<http://www.R-project.org/>). GSEA was performed as described in [44], using the publicly available desktop application from the Broad Institute (<http://www.broadinstitute.org/gsea/msigdb/downloads.jsp>). In particular, after gene



filtering, for all the datasets, probes were collapsed on Gene Symbols, again selecting for each Gene the probe with the largest mean expression across all the experiments. The data were analyzed for enrichment in biological themes (GO – Biological Processes, Molecular Functions, Cellular Components) using the Database for Annotation, Visualization and Integrated Discovery Bioinformatics Resources (DAVID, <http://david.abcc.ncifcrf.gov>). GSEA Enrichment statistics were performed with the default setting, based on Pearson metric. P-values and FDRs were calculated by repeating sample permutations 1000 times. 3D microarray data have been deposited in The Gene Expression Omnibus of the National Center for Biotechnology Information (accession number GSE81850).

#### 2.4 Statistical analyses

Data are expressed as mean  $\pm$  SD. Differences between groups were determined using a one-way analysis of variance with Kruskal-Wallis test. Significance between groups was established for  $p < 0.05$ .

### 3. Results

#### 3.1 NF- $\mu$ TP and CAF- $\mu$ TP production by dynamic culture: analysis of dimension, ECM deposition and cell growth during culture time

Before fabricating the heterotypic tumoral  $\mu$ TP, we investigated the behavior of normal fibroblasts (NF) and cancer-associated fibroblasts (CAF) in homotypic 3D cultures. As expected, CAF showed a higher level of  $\alpha$ -SMA, a specific biomarker of fibroblast differentiation and activation, than NF (Fig.S1a-b). In addition, qRT-PCR revealed an increased mRNA expression level in the CAF of both  $\alpha$ -SMA (60-fold) and SDF-1 (33-fold), a cancer-specific cytokine, which has been demonstrated to be up-regulated in CAF compared to NF [36,45] (Fig. S1c). Therefore, NF and CAF were used to produce homotypic  $\mu$ TP by their growth on gelatin microscaffolds in a spinner bioreactor, as described in Fig. 1. NF and CAF proliferation was analyzed by counting the number of cells *per* microtissue at day 1, 4, 8 and 12. Cell number increased about 5 times along 12 days, with a final ratio of about 1000 cells/microtissue (cells/ $\mu$ TP) both for NF and CAF (Fig 2a). We analyzed the dimensional evolution of  $\mu$ TP by evaluating their area at 4, 8 and 12 days. We observed that NF- $\mu$ TP did not show variations in the surface area during the 12 days of culture, while CAF- $\mu$ TP tended to contract after four days, showing a smaller surface than NF- $\mu$ TP area at day 12 (Fig 2b). By using NF and CAF carrying DsRed protein, the formation of NF- and CAF- $\mu$ TP was monitored by confocal microscopy at day 4, 8 and 12 (Fig S1d-i), showing the homogeneous distribution of growing cells and their aggregation to form a stromal microtissue, also due to the synthesis of endogenous ECM. At day 12 the dynamics cultures were interrupted and analyzed. The

expression of Ki-67 showed the distribution of the cells in active proliferation state in the stromal microtissue. Interestingly NFs were uniformly proliferating (Fig. 2c), while in CAF  $\mu$ TP cell growth was mainly observed at the periphery (Fig. 2d). We hypothesized that this different behavior could be justified by the different metabolism featuring CAF and NF. It is well known that CAFs have a faster metabolism [46] as consequence there are more cells in active proliferation state at the periphery of the microtissue to easily enter in contact with nutrients. The ECM of NF- and CAF- $\mu$ TP was further analyzed to detect the presence of collagenous and non-collagenous components. Masson's trichrome staining highlighted a much stronger collagen deposition in the ECM of CAF- $\mu$ TP compared to NF- $\mu$ TP (Fig 2e and 2f) and a corresponding more pronounced microscaffold degradation during culture time in the former compared to the latter (Fig. S2). Acid glycosaminoglycans stained by Alcian blue (Fig 2g,h) were more abundant in CAF- $\mu$ TP than in NF- $\mu$ TP. Of note PDAC desmoplastic reactions are enriched in these heteropolysaccharides [47]. Furthermore, the content of collagen and glycosaminoglycans (GAGs) was quantified and the results reported in the Fig. S3. Briefly, the content of collagen in CAF- $\mu$ TP was higher than in NF- $\mu$ TP ( $31.8 \pm 1.4$  % vs  $21.6 \pm 0.9$ %) (Fig. S3a), as well as the GAGs deposition area was larger in CAF- $\mu$ TP than in NF- $\mu$ TP ( $51.1 \pm 2.3$  % vs  $23.7 \pm 1.02$ %) (Fig. S3b).

### 3.2 NF- $\mu$ TP and CAF- $\mu$ TP over express ECM remodeling genes and down-regulate cell cycle gene compared to 2D culture

To gain further insight into the 3D  $\mu$ TP, we examined the phenotypes of NF and CAF performing cDNA microarray analyses to find global gene expression changes in 3D *versus* 2D culture. Two to three replicates were prepared *per* group and genes whose levels differed significantly after 12 days of culture among 3D and 2D were identified. Volcano plots show the changes in the  $\log_2$ -fold change and p-values for all genes differentially expressed in the separate comparisons of NF- $\mu$ TP and CAF- $\mu$ TP with respect to the relative 2D cultures (Fig 3a). LIMMA analysis [48] revealed that NF- $\mu$ TP had differential expression compared to the relative 2D cultures for 1845 probe sets (out of 19.842), where a difference was defined as a fold change ( $\log_2$ ) greater than 1 or less than -1 and a adjusted p-value less than 0.1 to achieve statistical and biological significance; among them, 1022 genes were up-regulated and 823 genes down-regulated. CAF- $\mu$ TP had differential expression compared to the relative 2D cultures for 456 probe sets (out of 17.849); 126 genes were up-regulated and 331 genes down-regulated. A large number of genes differentially expressed in NF- $\mu$ TP relative to NF 2D cultures changed in a similar manner in CAF- $\mu$ TP relative to CAF 2D cultures (Fig 3b). The prostaglandin-endoperoxide synthase 2 (PTGS2), the chemokine ligand 2 (CXCL2), the dermatopontin (DPT), the interleukin-8 (IL8), the matrix metalloproteinase-1



(MMP1) were among the most up-regulated genes in both NF- $\mu$ TP and CAF- $\mu$ TP (Table S2). However, a much larger cohort of genes changed in expression in NF- $\mu$ TP relative to NF 2D cultures than in CAF- $\mu$ TP relative to CAF 2D cultures (Fig 3b; Table S2). DAVID and GSEA analyses were carried out on microarray data set to identify associated biological processes and pathways [44]. The gene sets with significantly different expression (FDR < 0.01,  $p$  < 0.05) were picked up. Genes that were up-regulated in NF- $\mu$ TP compared with the relative 2D cultures showed enrichment in the Gene Ontology (GO) categories related to ECM remodeling (“extracellular matrix”, “proteinaceous extracellular matrix”, “biological adhesion”, “cell adhesion”, “collagen”, “extracellular matrix”; Table 1), while genes down-regulated in NF- $\mu$ TP were highly enriched in the gene set involved in cell cycle processes (“M phase”, “cell division”, “cell cycle phase”, “cell cycle”, “nuclear division”, “mitosis”, “M phase of mitotic cell”, “mitotic cell cycle”, “cell cycle process”; Table 1), suggesting that cells cultured in 2D proliferate more rapidly compared to cells cultured in 3D. In agreement, GSEA revealed enrichment of genes involved in ECM organization, and down-regulation of genes related to cell cycle process (Fig. 3c). Similar pathways were also found enriched (“proteinaceous extracellular matrix”, “extracellular matrix”, “biological adhesion”, “metallopeptidase activity”) or down-regulated (“cell cycle process”) in CAF- $\mu$ TP relative to CAF 2D cultures (Fig. S4a, Table S3). Matrix remodeling is a complex series of events that involve cell secretory properties (e.g. deposition of collagen), as well as secretion of proteases (e.g. MMPs). GSEA analysis highlighted the enrichment also for the metallopeptidase activity, in particular we found the up-regulation of MMP2, MMP3, MMP9, MMP14 in NF and CAF cultured in 3D condition, suggesting their involvement in the degradation of gelatin microcarriers (Fig S4b). Changes in cell structure in response to the dimensionality show that observed differences in morphology and organization in tissue-like structures are influenced by the underlying transcriptional profile. These results suggest that the 3D culture system provides a model that better mimics cell-ECM interactions compared to the traditional 2D monolayer. Microarray analysis reported that in NF and CAF the genes with the largest fold changes relative to 2D conditions belong to the family of the ECM components. Microarray results were confirmed by qRT-PCR for 9 genes related to ECM remodeling that were found up-regulated in NF- $\mu$ TP and CAF- $\mu$ TP compared to the relative 2D cultures. They include different collagens (COL6A1, COL16A1, COL18A1), matrix metallo-proteinases (MMP1, MMP2, MMP3, MMP14), IL8, and ITGA11 (Fig. 4a). At last, surnatants were analyzed by zymography to investigate the expression and secretion of MMPs (Fig 4b). We observed an over-expression of MMP2 and MMP9 in CAF- $\mu$ TP compared to NF- $\mu$ TP, which could have a role in the area differences between CAF- $\mu$ TP and

NF- $\mu$ TP (Fig. 2b). We hypothesized that the higher expression of MMPs correlates with a more marked of gelatin microscaffolds with consequent contraction of microtissues.

### 3.3 Morphology and gene profile of homotypic PT45 spinner culture

PT45 were grown on gelatin microcarriers, forming a homotypic microtissue (PT45- $\mu$ TP), which showed clear difference in morphology compared to CAF- $\mu$ TP and NF- $\mu$ TP. Indeed, PT45- $\mu$ TP were formed by single microscaffolds completely surrounded by PT45 that adhered layer by layer on the microcarrier surfaces and colonized their pores (Fig. 5a). In contrast to fibroblast microtissues, PT45- $\mu$ TP did not show SHG signal at multiphoton microscopy, indicating the absence of structured collagen (Fig. 5a), as further inferred by Masson's trichrome staining (Fig. 5b). Moreover, immunohistochemical staining for Ki-67 protein demonstrated that PT45 cells were in proliferating phase (Fig. 5c). PT45 cell number in  $\mu$ TP was about 350 per bead after 12 days (Fig. 5d). PT45- $\mu$ TP area was not modified (Fig 5e), and these microtissues did not aggregate to form a larger structures comprising cells and ECM.

Microarray analysis allowed us to identify 344 genes (out of 19.843), which were modulated in PT45- $\mu$ TP compared with 2D cultures. Specifically 207 genes were up-regulated and 137 genes down-regulated (Fig. S5). The functional significance of these genes was assessed using DAVID and GSEA. Interestingly, as we reported for NF- $\mu$ TP and CAF- $\mu$ TP, GO terms belonging to the various categories of cell cycle processes ("cell cycle", "cell cycle process", "cell cycle phase", "M phase", "mitotic cell cycle", "cell division") were significantly represented in the down-regulated gene group (Fig 5f and Table2). Regarding the up-regulated genes group, we found that up-regulated genes showed enrichment in the GO categories related to "extracellular region part", "MHC class I receptor activity" and "antigen processing and presentation of peptide antigen via MHC class I" (Table 2). According to the lack of structured collagen (Fig 5a-b), DAVID and GSEA analyses did not show any significant enrichment in the functional categories related to ECM composition or ECM remodeling was revealed among the up-regulated genes.

### 3.4 Development of 3D PDAC- $\mu$ TP

In order to closely mimic the *in vivo* conditions of PDAC, we developed a 3D heterotypic culture system that provided a microtissue model for studying the behaviors and the dynamic interaction between stroma and cancer cells.  $\mu$ TP were produced by adding PT45 on NF- or CAF- $\mu$ TP at day 6 of dynamic 3D culture, as reported in Figure 1. The heterotypic NF/PT45- $\mu$ TP and CAF/PT45- $\mu$ TP were investigated by evaluating cell proliferation, dimensional evolution, morphology and ECM composition. The number of NF and CAF reached the value of 5000 and 1000 cells/ $\mu$ TP, respectively. Moreover, the number of PT45 cells rapidly increased reaching a total of 5000

cells/ $\mu$ TP both in NF/PT45 and CAF/PT45- $\mu$ TP (Fig 6a-b). Area analysis of heterotypic microtissues was performed at day 4, 8 and 12 of dynamic culture. As previously reported (Fig 2b), CAF- $\mu$ TP were smaller than that of NF- $\mu$ TP at earlier time points (day 4 and 8). However the addition of PT45 cells to NF- $\mu$ TPs induced a contraction of the whole  $\mu$ TP (Fig. 6c). Therefore the areas of NF/PT45 and CAF/PT45- $\mu$ TP were similar at day 8, suggesting that PT45 cells were able to differentiate NF to CAF, which are known to shrink ECM [49]. Matrix deposition was evaluated by Masson's trichrome (Fig. 6d-e) and Alcian blue staining (Fig. 6f-g) showing compact and highly cellularized tissues, enriched in collagen and glycosaminoglycan deposition mainly localized in the inner part of the microtissues, corresponding to the stromal area. The phenomenon was evident both in CAF/PT45- $\mu$ TP and NF/PT45- $\mu$ TP demonstrating for the latter a desmoplastic reaction due to normal fibroblast activation in presence of pancreatic cancer cells. The expression of the proliferation markers Ki-67 was localized in the outer part of the  $\mu$ TPs, demonstrating that PT45 cells were in active proliferation both in NF/PT45- $\mu$ TP and CAF/PT45- $\mu$ TP (Fig. 6h-i).

The morphology of 3D microtissues and the distribution of fibroblasts and PT45 cells, respectively carrying DsRed and Zs-Green lentiviral vectors, were observed by confocal microscopy. The images (Fig. 6j and 6k) clearly show that PT45 were evenly localized throughout the  $\mu$ TP, interacting with NF or CAF, giving rise to a multicellular model of pancreatic cancer.

### **3.5 Dynamic crosstalk in NF/PT45- $\mu$ TP induces NF activation and the expression of PDAC desmoplastic markers**

To evaluate the functional cross-talk between stromal and cancer cells at gene level after 12 days, NF/PT45- $\mu$ TP and CAF/PT45- $\mu$ TP were dissociated and DsRed<sup>+</sup> (NF and CAF) or ZSGreen<sup>+</sup> (PT45) cells were FACS sorted (Fig. 7a). In NF/PT45- $\mu$ TP we found the 53% of the cells were DsRed<sup>+</sup> (NF) and the 46% ZsGreen<sup>+</sup> (PT45). In CAF/PT45- $\mu$ TP we found the 70%, of the cells were DsRed<sup>+</sup> (NF) and the 26% ZsGreen<sup>+</sup> (PT45). After the isolation from the 3D co-cultures we analyzed the gene expression profile of NF, CAF and PT45 cells. We observed that there was only 1 gene differentially expressed between NF and CAF isolated from NF/PT45- $\mu$ TP and CAF/PT45- $\mu$ TP, suggesting the activation of NF when co-cultured with PT45 in 3D conditions. These observations were supported by the immunohistochemistry evaluation of  $\alpha$ -SMA, PDGF $\beta$ r and vimentin in NF- $\mu$ TP and NF/PT45- $\mu$ TP that confirmed the up-regulation of these fibroblast activation markers in NF co-cultured with PT45 (Fig. S6).

Indeed, Venn diagram in Fig. 7b shows a larger number of genes differentially expressed between CAF and NF when cells are cultured in 2D (488 genes; 455 genes up-regulated and 33 down-regulated) or in 3D (365; 122 up-regulated and 243 down-regulated). Moreover, we analyzed the

signature of NF isolated from NF/PT45- $\mu$ TP by GSEA. Heatmap of the “extracellular matrix” gene set highlighted the up-regulated expression of a set of genes involved in the desmoplasia, a specific stromal reaction that has been associated with tumor progression and poor prognosis of PDAC [50]. In particular we observed the higher expression of COL1, COL3, MMP11, VCN, POSTN in NF isolated from NF/PT45- $\mu$ TP compared to the other conditions (NF in 2D; NF harvested from NF/PT45 in 2D and NF from NF- $\mu$ TP) (Fig. 7c). Similar results were obtained in CAF isolated from CAF/PT45- $\mu$ TP (Fig. S7a). Microarray results were confirmed by qRT-PCR for 6 genes (COL3, COL4, COL5, MMP11, VCN, POSTN) related to desmoplasia that were found up-regulated in NF isolated from NF/PT45- $\mu$ TP compared to the other conditions (NF in 2D; NF harvested from NF/PT45 in 2D and NF from NF- $\mu$ TP) (Fig. 7d). Versican (VCN) and periostin (POSTN) are among the genes of desmoplastic reaction that play a significant role in PDAC progression [51-55]. By immunofluorescence staining we found that the expression of VCN and POSTN were respectively ~3 and 2 fold higher in NF/PT45- $\mu$ TP than in NF- $\mu$ TP (VCN<sup>+</sup> % area, NF- $\mu$ TP:  $8.2 \pm 3.84\%$ ; NF/PT45- $\mu$ TP:  $20.1 \pm 2.62\%$ ;  $p < 0.001$ ; POSTN<sup>+</sup> % area, NF- $\mu$ TP:  $13.1 \pm 1.2\%$ ; NF/PT45- $\mu$ TP:  $25.9 \pm 1.7\%$ ;  $p < 0.001$ ) (Fig. 8a). Similar results were obtained in CAF/PT45- $\mu$ TP when stained for VCN and POSTN (Fig. S7 b-c). Taken together, these results clearly demonstrate the activation of NF in the co-culture system developed through the assessing of the desmoplastic markers. In order to deeper investigate the collagen deposition in 3D  $\mu$ TP, second harmonic generation (SHG) imaging was performed for the homotypic and heterotypic models (Fig 8b-e). Moreover the collagen fraction was also quantified in the four models, highlighting a stronger secretion of collagen in  $\mu$ TP where fibroblasts show an activated phenotype (Fig. 8f). Finally, we also investigated the correlation index obtained by the analysis of the different SHG signal detected by the four 3D models (Fig. 8g). By performing GLCM texture analysis, we evaluated the correlation length as a parameter indicating the roughness of the collagen matrix that can be correlated to the tumor progression. The values of correlation length obtaining for the PDAC- $\mu$ TP were higher in comparison to the normal homotypic NF- $\mu$ TP, strengthened the hypothesis of the presence of fibrosis pathways in the activated microtissues.

#### 4. Discussion

Most of the available models for cancer research still fail to mimic several important aspects of the tumor microenvironment, such as the presence of stroma cell populations and a complex ECM that guarantees crucial patho-physiological molecular cross-talks [2]. In this paper, we developed a 3D cancer model in which tumor cells interact with the endogenous ECM produced by fibroblasts in order to replicate the complex nature of human tumors and furnish, in a future perspective, a more

realistic testing platform for pre-clinical use. This provided a patho-physiological context, which more accurately replicated solid cancer microenvironment compared not only to monolayer cultures in 2D but also to 3D spheroids models [56-58]. Indeed the latter are often used to mimic tumor tissues, but they are usually composed of a single cell type and lacked an organized ECM. It is widely demonstrated that the crosstalk between tumor and stroma cells was made possible by the spatial architecture of the ECM where paracrine signals could be transmitted between the different cells [59]. However, the lack of a model sustaining 3D cell autonomous ECM formation is prejudicial to study the dynamical reciprocity between cells and extracellular space occurring *in vivo* during cancer formation and progression. PDAC is a paradigmatic example of the role of stromal component in dictating the progression diseases as well as the therapeutic approach to be followed. Actually PDAC is characterized by a prominent desmoplastic reaction, which compresses the vascular bed thus reducing drug delivery and recruitment of immune competent cells that could represent important targets in this cancer type [60]. The desmoplastic reaction is driven by quiescent pancreatic stellate cells, which are activated by cancer cells to acquire a myofibroblasts (or CAF) phenotype, expressing some markers as  $\alpha$ -SMA and PDGF $\beta$ r [61]. In our 3D tumor model, native ECM is present and can carry out its regulatory role in guiding cell activation and tissue formation. By using a co-culture system on gelatin porous microcarriers, PT45, a human PDAC cell line carrying mutated *KRAS*, *TP53* and *CDKN2* [62-65], and human fibroblasts exploit a scalable and reproducible method to prepare uniform 3D tumors. Along the dynamic culture, gelatin microcarriers are progressively digested by embedded cells, which autonomously produce ECM with the features of the desmoplastic reaction. The morphological, molecular and immunophenotypic analysis of homo- and heterotypic  $\mu$ TP demonstrated significant effects of the 3D architecture combined with the features of different cell types on the  $\mu$ TP growth rate and on the cellular transcriptional profiles. Furthermore, the dynamic cell culture condition used allows a non-invasive monitoring of culture progression and sampling for time-course studies in different conditions. Actually  $\mu$ TP constituted by fibroblasts alone grow and aggregate up to 350-400  $\mu$ m in diameter, remodel the gelatin scaffold by depositing new ECM that undergo contraction. It is well-known that activated fibroblasts sustain fibrotic response in tumor [66] and produce more ECM than normal fibroblasts: in our model these features are replicated by CAF- $\mu$ TP. The different degradation rate of porous scaffolds could be correlated with over synthesis of MMPs by the activated stromal cells, leading to ECM remodeling that can facilitate metastasis dissemination [67]. On the contrary, the size of PT45- $\mu$ TP does not increase along the dynamic culture as well as they do not form any aggregates, due to the lack of neo-synthesized ECM. As well, PT45 cells show poor capability of gelatin scaffold remodeling. These strong differences between fibroblast and tumor

cell  $\mu$ TP in remodeling ECM are supported by gene expression analysis, which does not show any significant modification of genes involved in fibrotic response in PT45- $\mu$ TP compared with NF- $\mu$ TP and CAF- $\mu$ TP. The most notable feature of heterotypic  $\mu$ TP is the appearance of the desmoplastic reaction, which occurs both with CAF and NF- $\mu$ TP, indicating that in our model PT45 are able to activate NF, as reported *in vivo* [68,69]. Transcriptional data show an up-regulation of the genes related to the ECM and desmoplastic reaction in NF/PT45- $\mu$ TP in comparison to NF- $\mu$ TP, clearly indicating the phenotypic change occurring in NF during 3D co-culture. In particular, the fibroblast activation in NF/PT45- $\mu$ TP is demonstrated by the over-expression of  $\alpha$ -SMA and PDGF $\beta$ r. The validation by qPCR and immunophenotypic staining of the microarray data in NF in homotypic and heterotypic cultures demonstrates the up-regulation of ECM-related genes, confirming that the heterotypic model fabricated is able to resemble both the genetic expression and the protein deposition that characterize the *in vivo* PDAC. Moreover, upon dissociation of heterotypic microtissues we found that cancer cells represented the predominant proportion of proliferating cells in agreement with other 3D co-cultured systems [70]. The morphology of NF/PT45- $\mu$ TP and CAF/PT45- $\mu$ TP are quite similar, demonstrating that -when co-cultured with PT45- both NF and CAF increase the deposition of endogenous matrix and glycosaminoglycans, mimicking the fibrotic microenvironment of pancreatic cancer [71]. Moreover the analysis based on SHG microscopy allows the quantification of ECM alteration that is routinely used to score collagen re-organization during tumoral progression *in vivo* [72-74]. The model we proposed is strengthened by the endogenous production and self-organization of ECM, leading to the presence of a more reliable dynamic interplay between cells and microenvironment. As a consequence, the correlation curve from GLCM analysis performed on unstained collagen network, led to the increase of the correlation length. This means that the collagen network we obtained in the PDAC model is quite similar to the architectural change due to stromal activation as happens *in vivo* in the case of pathological tissues [40,72-73]. This is a very important result, since so far no other *in vitro* tumor model allows to use this technique for analyzing ECM remodeling due to pathological events [74]. The observed ECM remodeling favors the invasion of the tumor cells into the  $\mu$ TP, mimicking the morphological features of PDAC, where myofibroblasts and cancer cells intimately connected to establish specific molecular cross-talks. Generally pancreatic CAFs release TGF $\beta$ , which triggers an invasive phenotype characterized by epithelial-mesenchymal, down-modulation E-cadherin, and up-regulation of the transcription factors Twist and Snail [75]. A common trait of 3D  $\mu$ TP is a reduced proliferative rate in comparison with 2D cultures, as previously described for other 3D tumor models [4,76]. The slower growth rates seen in 3D models more closely resemble those seen



*in vivo*, as a consequence of the restraints on energy availability within a solid structure [26]. As reported for homotypic  $\mu$ TP, gene expression analysis of the heterotypic culture of normal and CAFs with PT45 cells shows the down-regulation of the genes related to cell cycle, mitosis, cell division in 3D model in comparison to 2D cell culture, confirming a more physiological cells cycle in the 3D geometry. It is important to point out that the presence of the desmoplastic reaction that characterizes our heterotypic  $\mu$ TP has been previously demonstrated only when complex systems such as organoids from human PDAC were transplanted in recipient immune-compromised mice [77]. In conclusion, our results indicated that the established dynamic procedure allowed the development of PDAC  $\mu$ TP that mimic the capability of cancer cells to instruct stroma cells and reconstitute the desmoplastic reaction that characterizes the advanced stage of this neoplasia and affects drug delivery.

### **Conclusion**

In the light of these considerations PDAC  $\mu$ TP can represent a valuable tool to approach the molecular dynamics between stroma and tumor cells and to test drugs interrupting this deleterious circuit. The substitution of gelatin scaffold with endogenous ECM makes our model a novel and unique tool to investigate the real signals passing between stroma and tumor cells. The results of this work have important implications in the advancement of tissue-on-chip technology furnishing reliable *in vitro* disease models in which the ECM can carry out its role of key regulator of cell and tissue functions. At last, the tissue engineering approach used to produce PDAC  $\mu$ TP could be applied to cell lines and patient-derived primary cultures in order to reproduce different kinds of cancer models.

### **Acknowledgment**

We thank Valentina La Tilla for graphical support and Roberta Infranca for her precious and careful proofreading. Moreover we are grateful for financial support provided by the following grants: FIRB project Newton [RBAP11BYNP\_004] of the Italian Ministry of Education, University and Research (MIUR), AIRC [Grants 14284, 12182], Compagnia di San Paolo-University of Torino [Grant: Globreg] and Fondazione CRT [Grant : RF= 2015.2576].

### **Conflict of interest**

The authors have declared that there is no conflict of interest.

**References**

- [1] D. Huh, G.A. Hamilton, D.E. Ingber, From 3D cell culture to organs-on-chips. *Trends Cell Biol* 21 (2011) 745-54.
- [2] G. Imparato, F. Urciuolo, P.A. Netti, In vitro three-dimensional models in cancer research: a review. *Int Mat Rev* 60 (2015) 297-311.
- [3] E.C. Costa, V.M. Gaspar, P. Coutinho, P.J. Correia, Optimization of Liquid Overlay Technique to Formulate Heterogenic 3D Co-Cultures Models. *Biotechnol Bioeng* 111 (2014) 1672-85.
- [4] A. Nyga, M. Loizidou, M. Emberton, U. Cheema, A novel tissue engineered three-dimensional in vitro colorectal cancer model. *Acta Biomater* 9 (2013) 7917-26.
- [5] C.T. Tsao, F.M. Kievit, K. Wang, A.E. Erickson, Richard G. Ellenbogen, and M. Zhang. Chitosan-Based Thermoreversible Hydrogel as an in Vitro Tumor Microenvironment for Testing Breast Cancer Therapies. *Mol Pharmaceutics* 11 (2014) 2134-2142
- [6] P. DelNero, M. Lane, S.S. Verbridge, B. Kwee, P. Kermani, B. Hempstead, A. Stroock, C. Fischbach. "3D culture broadly regulates tumor cell hypoxia response and angiogenesis via pro-inflammatory pathways", *Biomaterials* 55 (2015) 110-118
- [7] N. Peela, F.S. Sam, W. Christenson, D. Truong, A.W. Watson, G. Mouneimne, R. Ros, M. Nikkhah. A three dimensional micropatterned tumor model for breast cancer cell migration studies. *Biomaterials* 81 (2016) 72-83
- [8] Y.C. Chen, X. Lou, Z. Zhang, P. Ingram and E. Yoon. High-Throughput Cancer Cell Sphere Formation for Characterizing the Efficacy of Photo Dynamic Therapy in 3D Cell Cultures. *Sci Rep* 5 (2015) doi: 10.1038/srep12175
- [9] X. Fang, S. Sittadjody, K. Gyabaah, E.C. Opara, K.C. Balaji. Novel 3D Co-Culture Model for Epithelial-Stromal Cells Interaction in Prostate Cancer. *PLoS ONE* 8 (2013): e75187 doi:10.1371/journal.pone.0075187
- [10] P. Yeung, H.S. Sin, S. Chan, G.C.F. Chan, B.P. Chan. Microencapsulation of Neuroblastoma Cells and Mesenchymal Stromal Cells in Collagen Microspheres: A 3D Model for Cancer Cell Niche Study, *PLoS ONE* 10(2015) doi:10.1371/ journal.pone.0144139
- [11] S.J. Horning, D.A. Haber, W.K.D. Selig, S.P. Ivy, S.A. Roberts, J.D. Allen, E.V. Sigal, C.L. Sawyers. Developing standards for breakthrough therapy designation in oncology. *Clin Cancer Res* 15 (2013) 4297-304.
- [12] C. Fischbach, R. Chen, T. Matsumoto, T. Schmelzle, J.S. Brugge, P.J. Polverini, Engineering tumors with 3D scaffolds, *Nat Methods* 4 (2007) 855-60.



- [13] T.M. Achilli, J. Meyer, J.R. Morgan, Advances in the formation, use and understanding of multi-cellular spheroids. *Expert Opin Biol Ther.* 12 (2012) 1347-60.
- [14] M.F. Estrada, S.P. Rebelo, E.J. Davies, M.T. Pinto, H. Pereira, V.E. Santo, M.J. Smalley, S.T. Barry, E.J. Gualda, P.M. Alves, E. Anderson, C. Brito, Modelling the tumour microenvironment in long-term microencapsulated 3D co-cultures recapitulates phenotypic features of disease progression, *Biomaterials* 78 (2016) 50-61.
- [15] C. Ricci, L. Moroni, S. Danti, Cancer tissue engineering-new perspectives in understanding the biology of solid tumours-a critical review. *OA Tissue Engineering* 1 (2013) 1-4.
- [16] F.E.M. Froeling, T.A. Mirza, R.M. Feakins, A. Seedhar, G. Elia, I.R. Hart, H.M. Kocher. Organotypic culture model of pancreatic cancer demonstrates that stromal cells modulate E-Cadherin,  $\beta$ -Catenin, and Ezrin expression in tumor cells. *Am J Pathol* 175 (2009) 636–648
- [17] C. Neuzillet, A. Tijeras-Raballand, P. Bourget, J. Cros, A. Couvelard, A. Sauvanet, M.P. Vullierme, C. Tournigandc, P. Hammel, State of the art and future directions of pancreatic ductal adenocarcinoma therapy. *Pharmacol Ther* 155 (2015) 80-104.
- [18] S.J. Coleman, J. Watt, P. Arumugam, L. Solaini, E. Carapuca, M. Ghallab, R.P. Grose, H.M. Kocher. Pancreatic cancer organotypics: High throughput, preclinical models for pharmacological agent evaluation. *World J Gastroenterol* 20 (2014) 8471–481.
- [19] L. Rahib, B.D. Smith, R. Aizenberg, A.B. Rosenzweig, J.M. Fleshman, L.M. Matrisian. Projecting cancer incidence and deaths to 2030: the unexpected burden of thyroid, liver, and pancreas cancers in the United States. *Cancer Res* 74 (2014) 2913–21.
- [20] R. Cohen, C. Neuzillet, A. Tijeras-Raballand, S. Faivre, A. de Gramont, E. Raymond Targeting cancer cell metabolism in pancreatic adenocarcinoma. *Oncotarget* 10 (2015) 16832-47
- [21] C. Feig, A. Gopinathan, A. Neesse, D.S. Chan, N. Cook, D.A. Tuveson. The Pancreas Cancer Microenvironment. *Clin Cancer Res* 18 (2012) 4266-76.
- [22] G.C. Chu, A.C. Kimmelman, A.F. Hezel, R.A. DePinho, Stromal biology of pancreatic cancer. *J Cell Biochem* 101 (2007) 887-907.
- [23] Y. Liu , F. Li, F. Gao, L. Xing, P. Qin , X. Liang , J. Zhang, X. Qiao, L. Lin, Q. Zhao, L. Du. Role of microenvironmental periostin in pancreatic cancer progression. *Oncotarget* 23 (2016) doi: 10.18632/oncotarget.11533.
- [24] M.A. Shields, S. Dangi-Garimella, A.J. Redig, H.G. Munshi, Biochemical role of the collagen-rich tumour microenvironment in pancreatic cancer progression. *Biochem J* 15 (2012) 541-52.
- [25] P. Olson, D. Hanahan, Breaching the Cancer Fortress. *Science* 324 (2009) 1400-1.

- [26] T.P. Padera, B.R. Stoll, J.B. Tooredman, D. Capen, E. di Tomaso, R.K. Jain. Pathology: Cancer cells compress intratumor vessels. *Nature* 427 (2004) 695.
- [27] P. Longati, X. Jia, J. Eimer, A. Wagman, M.R. Witt, S. Rehnmark, C. Verbeke, R. Toftgård, M. Löhr, R.L. Heuchel. 3D pancreatic carcinoma spheroids induce a matrix-rich, chemoresistant phenotype offering a better model for drug testing. *BMC Cancer* 13 (2013) 95.
- [28] Y. Miki, K. Ono, S. Hata, T. Suzuki, H. Kumamoto, H. Sasano, The advantages of co-culture over mono cell culture in simulating in vivo environment. *J Steroid Biochem Mol Biol* 131 (2012) 68-75.
- [29] G. Imparato, F. Urciuolo, C. Casale, P.A. Netti. The role of microsccaffold properties in controlling the collagen assembly in 3D dermis equivalent using modular tissue engineering. *Biomaterials* 34 (2013) 7851-61.
- [30] H. Kalthoff, W. Schmiegel, C. Roeder, D. Kasche, A. Schmidt, G. Lauer, H.G. Thiele, G. Honold, K. Pantel, G. Riethmuller. p53 and K-RAS alterations in pancreatic epithelial cell lesions. *Oncogene* 8 (1993) 289-298.
- [31] P.S. Moore, B. Sipos, S. Orlandini, C. Sorio, F.X. Real, N.R. Lemoine, T. Gress, C. Bassi, G. Klöppel, H. Kalthoff, H. Ungefroren, M. Löhr, A. Scarpa, Genetic profile of 22 pancreatic carcinoma cell lines Analysis of K-ras, p53, p16 and DPC4/Smad4. *Virchows Arch* 439 (2001) 798–802
- [32] D. D'Eliseo, L. Manzi, N. Merendino, F. Velotti, Docosahexaenoic acid inhibits invasion of human RT112 urinary bladder and PT45 pancreatic carcinoma cells via down-modulation of granzyme B expression. *J Nutr Biochem* 23 (2012) 452–457
- [33] B. Vizio, F. Biasi, T. Scirelli, A. Novarino, A. Prati, L. Ciuffreda, G. Montrucchio, G. Poli, G. Bellone, Pancreatic-carcinoma-cell-derived pro-angiogenic factors can induce endothelial-cell differentiation of a subset of circulating CD34+ progenitors. *J Transl Med* 11 (2013) 314
- [34] F. Gioiella, F. Urciuolo, G. Imparato, V. Brancato. An engineered breast cancer model on a chip to replicate ECM-activation in vitro during tumor progression. *Adv Healthcare Mater* (2016) DOI: 10.1002/adhm.201600772
- [35] K. Nilsson, F. Buzsaky, K. Mosbach. Growth of anchorage-dependent cells on macroporous microcarriers. *Nat Biotechnol* 4 (1986) 989-90.
- [36] Y. Kojima, A. Acar, E.N. Eaton, K.T. Mellody, C. Scheel, I. Ben-Porath, T.T. Onder, Z.C. Wang, A.L. Richardson, R.A. Weinberg, A. Orimo, Autocrine TGF- $\beta$  and stromal cell-derived factor-1 (SDF-1) signaling drives the evolution of tumor promoting mammary stromal myofibroblasts. *Proc Natl Acad Sci U S A*. 107 (2010) 20009-14.

- [37] A. Sadlonova, Z. Novak, M. R. Johnson, D. B. Bowe, S. R. Gault, G. P. Page, J. V. Thottassery, D. R. Welch, A. R. Frost. Breast fibroblasts modulate epithelial cell proliferation in three-dimensional in vitro co-culture. *Breast Cancer Research* 7 (2004) 46 doi: 10.1186/bcr949
- [38] A. E. Hegab, D. Arai, J. Gao, A. Kuroda, H. Yasuda, M. Ishii, K. Naoki, K. Soejima, T. Betsuyaku. Mimicking the niche of lung epithelial stem cells and characterization of several effectors of their in vitro behavior. *Stem Cell Research* 15 (2015) 109-21 doi.org/10.1016/j.scr.2015.05.005
- [39] F. Urciuolo, A. Garziano, G. Imparato, V. Panzetta, S. Fusco, C. Casale, P.A. Netti. Biophysical properties of dermal building-blocks affect extra cellular matrix assembly in 3D endogenous macro-tissue. *Biofabrication* 8 (2016) 015010.
- [40] G. Imparato, C. Casale, S. Scamardella, F. Urciuolo, M. Bimonte, F. Apone, G. Colucci, P.A. Netti, A novel engineered dermis for *in vitro* photodamage research. *J Tissue Eng Regen Med*, 2016, DOI: 10.1002/term.2125.
- [41] L. Fu, E. Medico. FLAME, a novel fuzzy clustering method for the analysis of DNA microarray data. *BMC Bioinf* 8 (2007) 3.
- [42] G.K. Smyth, Linear models and empirical bayes methods for assessing differential expression in microarray experiments. *Stat Appl Genet Mol Biol* 3 (2004)
- [43] Y. Benjamini, Y. Hochberg, Controlling the False Discovery Rate: A Practical and Powerful Approach to Multiple Testing. *J R Stat Soc Series B Stat Methodol* 57 (1995) 289-300.
- [44] A. Subramanian, P. Tamayo, V.K. Mootha, S. Mukherjee, B.L. Ebert, M.A. Gillette, A. Paulovich, S.L. Pomeroy, T.R. Golub, E.S. Lander, J.P. Mesirov. Gene set enrichment analysis: a knowledge-based approach for interpreting genome-wide expression profiles. *Proc Natl Acad Sci U S A*. 102 (2005) 15545-50.
- [45] A. Orimo, P.B. Gupta, D.C. Sgroi, F. Arenzana-Seisdedos, T. Delaunay, R. Naeem, V.J. Carey, A.L. Richardson, R.A. Weinberg. Stromal fibroblasts present in invasive human breast carcinomas promote tumor growth and angiogenesis through elevated SDF-1/CXCL12 secretion. *Cell* 121 (2005) 335-48.
- [46] S. Pavlides, D. Whitaker-Menezes, R. Castello-Cros, N. Flomenberg, A. K. Witkiewicz, P. G. Frank, M. C. Casimiro, C. Wang, P. Fortina, S. Addya, R. G, Pestell, U. E. Martinez-Outschoorn, F. Sotgia, M. P. Lisanti, The reverse Warburg effect: Aerobic glycolysis in cancer associated fibroblasts and the tumor stroma, *Cell Cycle* 8 (2009) 3984-01.
- [47] E.E. Merika, K.N. Syrigos, M.W. Saif. Desmoplasia in pancreatic cancer. Can we fight it? *Gastroenterol Res Pract* (2012) 781765 doi: 10.1155/2012/781765..

- [48] Smyth GK. Limma: linear models for microarray data. In: R.Gentleman VCS DRIWH, ed. *Bioinformatics and Computational Biology Solutions using R and Bioconductor*. New York: Springer, 2005 397- 420
- [49] F. Calvo, N. Ege, A. Grande-Garcia, S. Hooper, R.P. Jenkins, S.I. Chaudhry, K. Harrington, P. Williamson, E. Moeendarbary, G. Charras, E. Sahai. Mechanotransduction and YAP-dependent matrix remodeling is required for the generation and maintenance of cancer-associated fibroblasts *Nat Cell Biol* 15 (2013) 637–646
- [50] M. Schober, R. Jesenofsky, R. Faissner, C. Weidenauer, W. Hagmann, P. Michl, R.L. Heuchel, S.L. Haas, J.M. Löhr. Desmoplasia and chemoresistance in pancreatic cancer. *Cancers* 6 (2014) 2137-54
- [51] C. Ricciardelli, A.J. Sakko, M.P. Ween, D.L. Russell, D.J. Horsfall. The biological role and regulation of versican levels in cancer. *Cancer Metastasis Rev.* 28 (2009) 233-45
- [52] S. Pan, R. Chen, T. Stevens, M.P. Bronner, D. May, Y. Tamura, M.W. McIntosh, T.A. Brentnall, Proteomics portrait of archival lesions of chronic pancreatitis *PLoS ONE* 6 (2011) :e27574
- [53] J. Koninger, M. Kanamori, H. Konno, N. Osato, J. Kawai, Y. Hayashizaki, H. Suzuki, A genome- wide and nonredundant mouse transcription factor database. *Biochem Biophys Res Commun* 322 (2004) 787-93
- [54] P. Baril, R. Gangeswaran, P.C. Mahon, K. Caulee, H.M. Kocher, T. Harada, M. Zhu, H. Kalthoff, T. Crnogorac-Jurcevic, N.R. Lemoine. Periostin promotes invasiveness and resistance of pancreatic cancer cells to hypoxia-induced cell death: role of the beta4 integrin and the PI3k pathway. *Oncogene* 26 (2007) 2082-94.
- [55] Y. Liu, L. Du, Role of pancreatic stellate cells and periostin in pancreatic cancer progression. *Tumour Biol* 36 (2015) 3171-7.
- [56] B.M. Holzapfel, J.C Reichert, J.T. Schantz, U. Gbureck, L. Rackwitz, U. Nöth, F. Jakob, M. Rudert, J. Groll D. W. Hutmacher. How smart do biomaterials need to be? A translational science and clinical point of view. *Adv Drug Deliv Rev* 65 (2013) 581-603.
- [57] L.B. Weiswald, D. Bellet, V. Dangles-Marie. Spherical Cancer Models in Tumor Biology *Neoplasia* 17 (2015) 1–15.
- [58] D.W. Infanger, M.E. Lynch, C. Fischbach. Engineered culture model for studies of Tumor-Microenvironment Interaction. *Annu Rev Biomed Eng* 15 (2013) 29–53.
- [59] K. Ashlee, A.K. Clark, A.V. Taubenberger, R.A. Taylor, B. Niranjana, E.Y. Chea. A bioengineered microenvironment to quantitatively measure the tumorigenic properties of cancer associated fibroblast in human prostate cells. *Biomaterials* 34 (2013) 4777-85

- [60] Y. Zhu, B.L. Knolhoff, M.A. Meyer, T.M. Nywening, B.L. West, J Luo, A. Wang-Gillam, S.P. Goedegebuure, D.C. D.C. Linehan, D.G. DeNardo. CSF1/CSF1R blockade reprograms tumor-infiltrating macrophages and improves response to T-cell checkpoint immunotherapy in pancreaticcancer models. *Cancer Res.* 15 (2014) 5057-69.
- [61] E.F. Carapuça, E. Gemenetzidis, C. Feig, T.E. Bapiro, M.D. Williams, A.S. Wilson, F.R. Delvecchio, P. Arumugam, R.P. Grose, N.R. Lemoine, F.M. Richards, H.M. Kocher. Anti-stromal treatment together with chemotherapy targets multiple signalling pathways in pancreatic adenocarcinoma. *J Pathol* (2016) doi: 10.1002/path.4727
- [62] D.P. Ryan, T.S. Hong, N. Bardeesy. Pancreatic adenocarcinoma. *N Engl J Med* 11 (2014) 1039-49.
- [63] R. Kalluri, M. Zeisberg. Fibroblasts in cancer. *Nat Rev Cancer.* 6 (2006) 392-401.
- [64] P.S. Moore, B. Sipos, S. Orlandini, C. Sorio, F.X. Real, N.R. Lemoine, T. Gress, C. Bassi, G. Klöppel, H. Kalthoff, H. Ungefroren, M. Löhr, A. Scarpa. Genetic profile of 22 pancreatic carcinoma cell lines *Virchows Arch* 439 (2001) 798-802.
- [65] P. Monti, F. Marchesi, M. Reni, A. Mercalli, V. Sordi, A. Zerbi, G. Balzano, V. Di Carlo, P. Allavena, L.A. Piemonti comprehensive in vitro characterization of pancreatic ductal carcinoma cell line biological behavior and its correlation with the structural and genetic profile. *Virchows Arch* 445 (2004) 236-247
- [66] T.S. Mantoni, S. Lunardi, O. Al-Assar, A. Masamune, T.B. Brunner. Pancreatic stellate cells radioprotect pancreatic cancer cells through  $\beta 1$ -integrin signaling. *Cancer Res* 71 (2011) 3453–3458
- [67] Y. Xu, Z. Li, P. Jiang, G. Wu, K. Chen, X. Zhang, X. Li. The co-expression of MMP-9 and Tenascin-C is significantly associated with the progression and prognosis of pancreatic cancer. *Diagn Pathol* 10 (2015) 211.
- [68] L.A. Gurski, N.J. Petrelli, X. Jia, M.C. Farach-Carson, 3D Matrices for Anti-Cancer Drug Testing and Development. *Oncol Issues* 1 (2010) 20-25.
- [69] O.M. Maria, O. Maria, Y. Liu, S.V. Komarova, S.D. Tran. Matrigel improves functional properties of human submandibular salivary gland cell line. *Int J Biochem Cell Biol* 43 (2011) 622–631
- [70] M. Majety, L.P. Pradel, M. Gies, C.H. Ries. Fibroblasts Influence Survival and Therapeutic Response in a 3D Co-Culture Model. *PLoS ONE* 10 (2015) doi:10.1371/journal.pone.0127948.
- [71] M. Erkan Understanding the stroma of pancreatic cancer: co-evolution of the microenvironment with epithelial carcinogenesis. *J Pathol* 231 (2013) 4–7.

- [72] C.B. Raub, V. Suresh, T. Krasieva, J. Lyubovitsky, J.D. Mih, A.J. Putnam, B.J. Tromberg, S.C. George. Non-invasive assessment of collagen gel microstructure and mechanics using multiphoton microscopy. *Biophys J* 92 (2007) 2212–2222.
- [73] S. Zhuo, J. Chen, G. Wu, Quantitatively linking collagen alteration and epithelial tumor progression by second harmonic generation microscopy. *Appl Phys Lett* 96 (2010) 213704.
- [74] S. Zhuo, J.Chen, S. Xie, Z. Hong and X. Jiang. Extracting diagnostic stromal organization features based on intrinsic two-photon excited fluorescence and second-harmonic generation signals. *J Biomed Opt* 14 (2009) doi: 10.1117/1.3088029
- [75] A. Makohon-Moore, C. A. Iacobuzio-Donahue, Pancreatic cancer biology and genetics from an evolutionary perspective *Nature Rev Cancer* 16 (2016) 553-565.
- [76] F.M. Kievit, S.J. Florczyk, M.C. Leung, O. Veiseh, J.O. Park, M.L. Disis, M. Zhang, Chitosan-alginate 3D scaffolds as a mimic of the glioma tumor microenvironment. *Biomaterials* 31 (2010) 5903-10
- [77] S.F. Boj, C.I. Hwang, L.A. Baker, I.I. Chio, D.D. Engle, V. Corbo, M. Jager, M. Ponz-Sarvisé, H.Tiriác, M.S. Spector, A. Gracanin, T. Oni, K.H. Yu, R. van Boxtel, M. Huch, K.D. Rivera, J.P. Wilson, M.E. Feigin, D. Öhlund, A. Handly-Santana, C.M. Ardito-Abraham, M. Ludwig, E. Elyada, B. Alagesan, G. Biffi, G.N. Yordanov, B. Delcuze, B. Creighton, K. Wright, Y. Park, F.H. Morsink, I.Q. Molenaar, I.H. Borel Rinkes, E. Cuppen, Y. Hao, Y. Jin, I.J. Nijman, C. Iacobuzio-Donahue, S.D. Leach, D.J. Pappin, M. Hammell, D.S. Klimstra, O. Basturk, R.H. Hruban, G.J. Offerhaus, R.G. Vries, H. Clevers. Organoid models of human and mouse ductal pancreatic cancer *Cell* 15 (2015) 324-38.



**Fig.1 Schematic representation of the process designed for developing the 3D *in vitro* PDAC model.** Normal or cancer associated fibroblast were combined with gelatin micro scaffold in a spinner bioreactor in order to generate stromal microtissues. After 6 days of dynamic culture, pancreatic cancer cells were added and the culture was stopped at day 12 for collecting PDAC microtissues in order to perform further investigations.

**Fig.2 Stromal  $\mu$ TP production and characterization.** (a) Cell proliferation in homotypic 3D culture at day 1, 4, 8 and 12. (b) Dimensional analysis was performed calculating the area evolution of the stromal microtissues at day 4, 8 and 12. (c) Ki-67 IHC for NF and (d) CAF, scale bar is 50  $\mu$ m. Collagen deposition stained by Masson Trichrome in (d) NF- and (e) CAF- $\mu$ TP. Detection of glycosaminoglycans by Alcian Blu staining: in (f) NF- and (g) CAF- $\mu$ TP. Scale bar 50 $\mu$ m. Statistical significance, \* $p < 0.05$ . All images are referred to  $\mu$ TP at day 12 of culture.

**Fig.3 Microarray analyses of NF- and CAF- $\mu$ TP.** (a) Volcano plots of gene expression showing fold-change and p-value of NF- and CAF- $\mu$ TP *versus* their 2D cultures; up-regulated and down-regulated genes are colored red and blue, respectively. (b) Venn diagram showing the overlapping subsets of differentially expressed genes ( $|\log_2 FC| \geq 1$ , adjusted p-value  $< 0.1$  in the NF- and CAF- $\mu$ TP). (c) Enrichment plot relative to “extracellular matrix”, “metallopeptidase activity” and “cell cycle process” pathways for NF- $\mu$ TP *versus* 2D culture, found enriched by GSEA analysis of microarray data. Normalized enrichment scores (NESs), p and q values are shown.

**Fig.4 ECM remodeling and MMPs secretion quantification.** (a) qRT-PCR validation of significantly modulated genes in NF- and CAF- $\mu$ TP;  $n = 3$ . Error bars indicate SEMs. (b) MMPs secretion analyzed by zymography assay in NF- and CAF- $\mu$ TP, at day 12 of dynamic culture.

**Fig.5 PT45- $\mu$ TP production and characterization.** (a) Confocal imaging of PT45- $\mu$ TP, scale bar is 75  $\mu$ m. (b) Masson Trichrome and (c) Ki-67 IHC staining of PT45- $\mu$ TP, scale bar is 50  $\mu$ m. All images are representative of day 12 of dynamic culture. (d) Cell proliferation and (e) area analysis of PT45- $\mu$ TP at day 1, 4, 8, 12. (f) Enrichment plot relative to “cell cycle process” pathway for PT45- $\mu$ TP *versus* 2D culture, found enriched by GSEA analysis of microarray data. Normalized enrichment scores (NESs), p and q values are shown.

**Fig.6 Characterization of PDAC- $\mu$ TP.** (a) Cell proliferation of NF/PT45- $\mu$ TP and (b) CAF/PT45- $\mu$ TP at days 1, 6, 7, 9 and 12 of culture. (c) Area analysis for NF/PT45- $\mu$ TP and CAF/PT45- $\mu$ TP at days 1, 4, 8 and 12 of 3D co-culture. Masson Trichrome staining for (d) NF/PT45- $\mu$ TP and (e) CAF/PT45- $\mu$ TP. Alcian Blu staining for (f) NF/PT45- $\mu$ TP and (g) CAF/PT45- $\mu$ TP. Ki-67 IHC for (h) NF/PT45- $\mu$ TP and (i) CAF/PT45- $\mu$ TP, scale bar is 50  $\mu$ m. Confocal imaging for (j) NF/PT45- $\mu$ TP and (k) CAF/PT45- $\mu$ TP. Scale bar 75  $\mu$ m. All images are referred to  $\mu$ TP at day 12 of culture.

**Fig.7 Gene expression profile, by microarray technique of PDAC- $\mu$ TP.** (a) Due to different infection of pancreatic and stromal cells, a cell sorting of co-cultured microtissues were performed before performing microarray. (b) Venn diagram showing the overlapping subsets of differentially expressed genes ( $|\log_2 FC| \geq 1$ , adjusted p-value  $< 0.1$ ). In clockwise direction: 2D culture of CAF *versus* 2D culture of NF, CAF from CAF- $\mu$ TP *versus* NF- $\mu$ TP, CAF from CAF/PT45- $\mu$ TP *versus* NF from NF/PT45- $\mu$ TP. (c) Heatmap of the GSEA “extracellular matrix” core gene set from NF/PT45  $\mu$ TP *versus* NF 2D, NF/PT45 2D, NF  $\mu$ TP conditions. (d) qRT-PCR validation of gene

expression changes in NF 2D, NF/PT45 2D, NF- $\mu$ TP and NF/PT45- $\mu$ TP; n = 3. Error bars indicate SEMs.

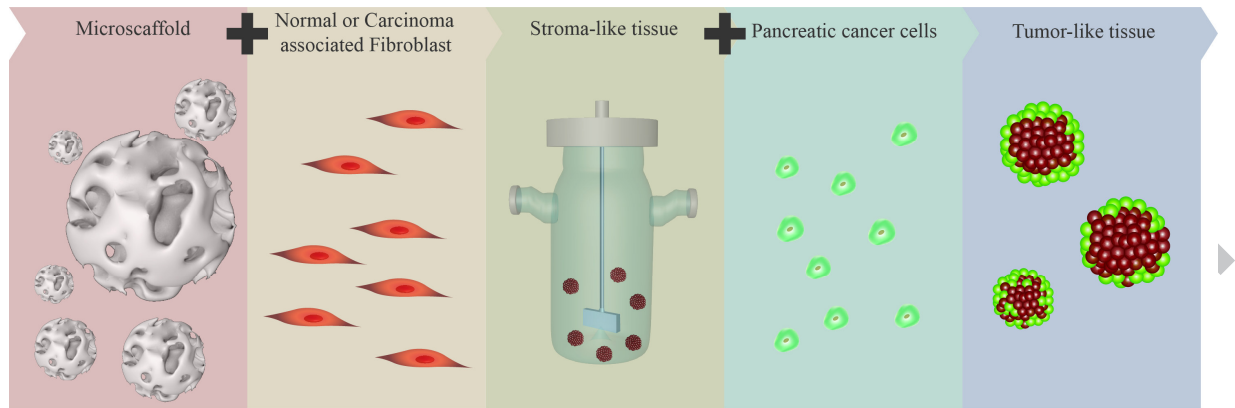
**Fig.8 Array validation by IF and SHG analysis of Collagen in  $\mu$ TP.** (a) VCN (red staining) and POSTN (green staining) IF and relative quantification analysis on NF- $\mu$ TP and NF/PT45- $\mu$ TP; nuclei were stained by DAPI in blue and scale bar is 75  $\mu$ m. All images are referred to  $\mu$ TP at day 12 of culture. SHG signal (gray scale) from newly formed fibrillar collagen in NF- $\mu$ TP (b), CAF- $\mu$ TP (c) and NF/PT45- $\mu$ TP (d) and CAF/PT45- $\mu$ TP (e). Scale bar = 75  $\mu$ m. All images are referred to  $\mu$ TP at day 12 of culture. SHG signal quantification analysis as collagen fraction % (e) in homotypic and heterotypic fraction. Correlation curve (f) as a function of distance in  $\mu$ m in homotypic and heterotypic culture at day 12 of culture. Correlation length -  $\lambda$  - obtained by fitting parameters from normalized correlation curves in homotypic and heterotypic culture at day 12 of dynamic culture (g). Line and asterisks indicate statistical differences with  $p < 0.05$ .

**Table 1. Molecular pathways found enriched by DAVID analysis of microarray data.** Up-regulated and down-regulated GO terms of NF- $\mu$ TP *versus* NF in 2D condition.

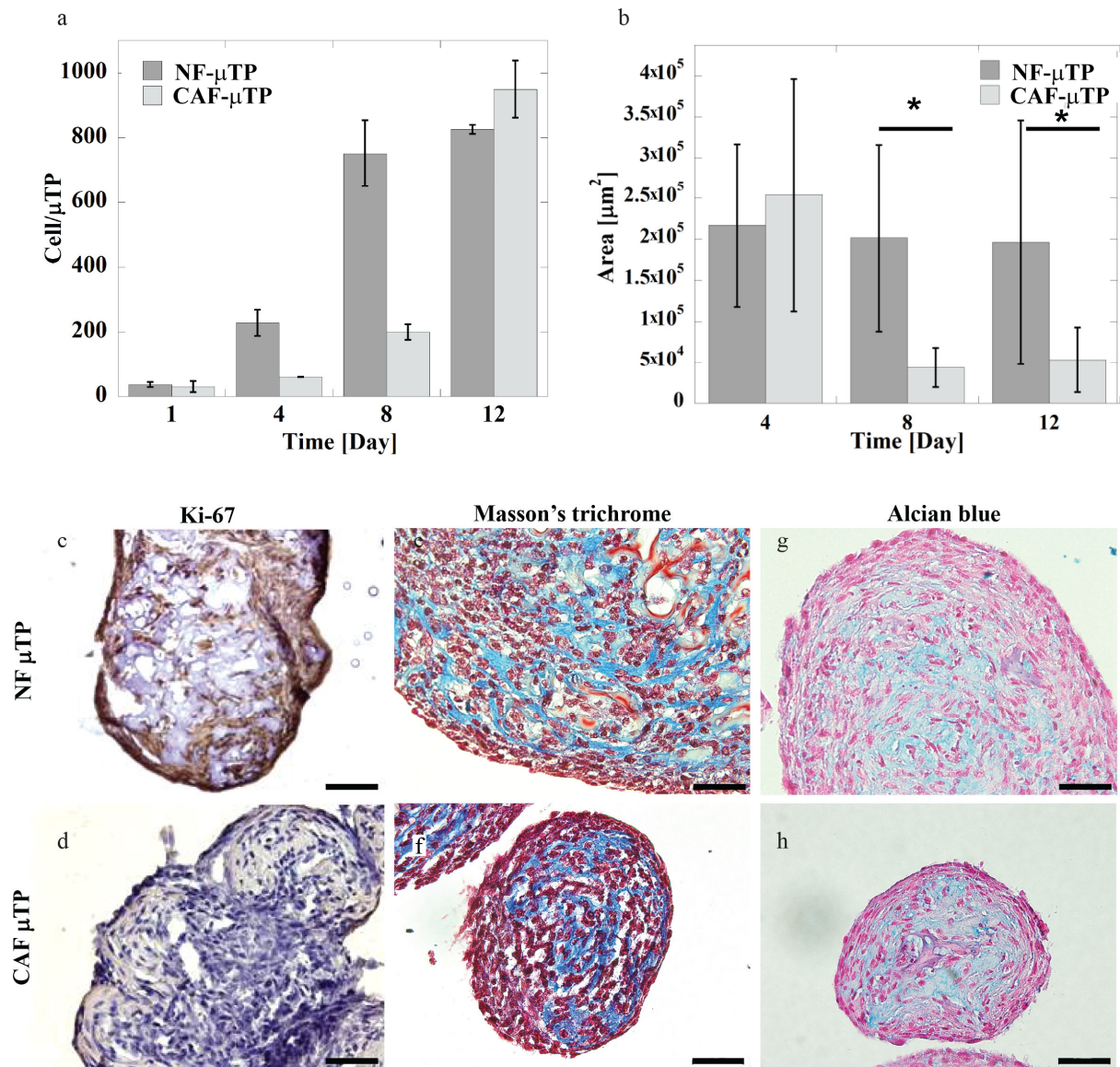
**Table 2. Molecular pathways found enriched by DAVID analysis of microarray data.** Up-regulated and down-regulated GO terms of PT45-  $\mu$ TP *versus* PT45 in 2D condition.

ACCEPTED MANUSCRIPT

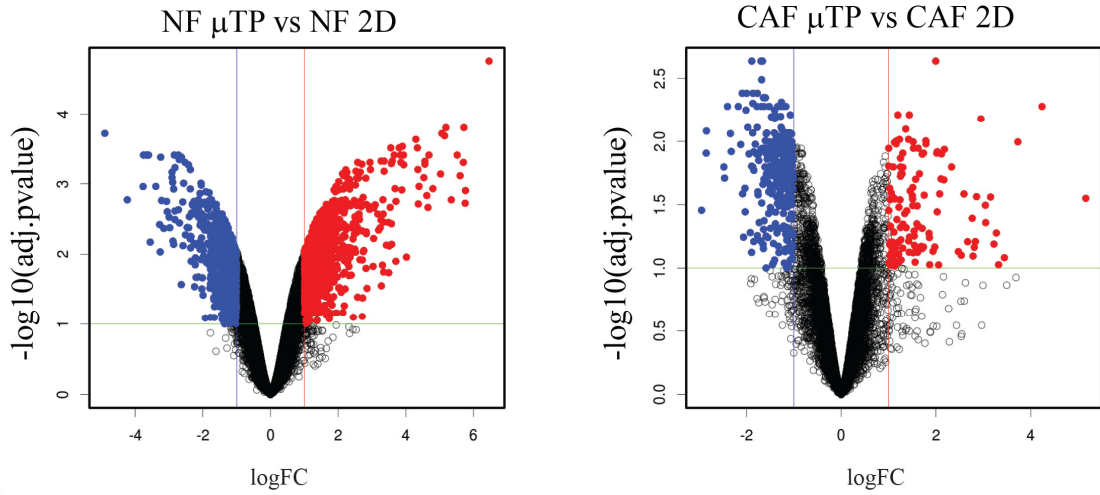




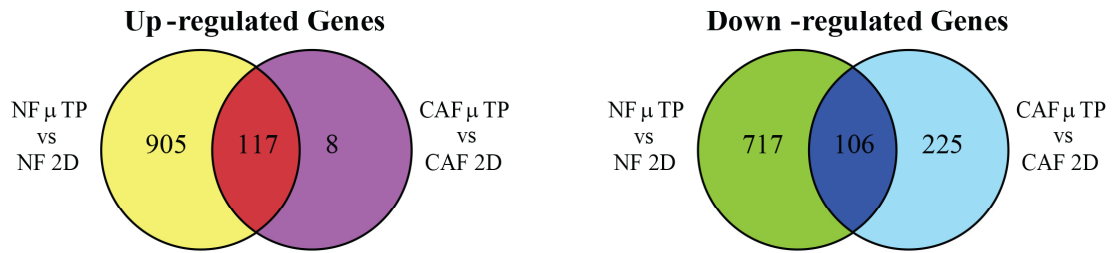
ACCEPTED MANUSCRIPT



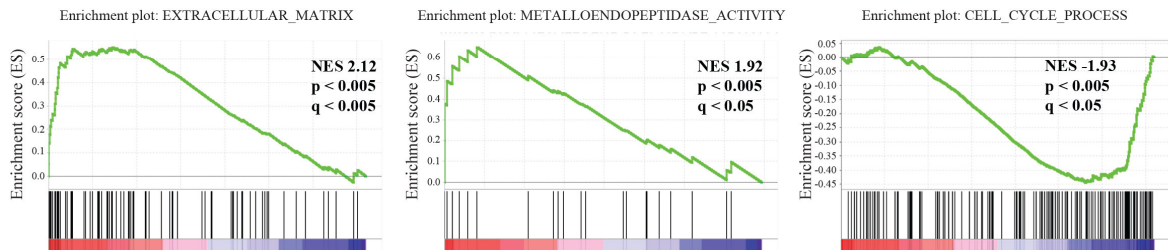
a

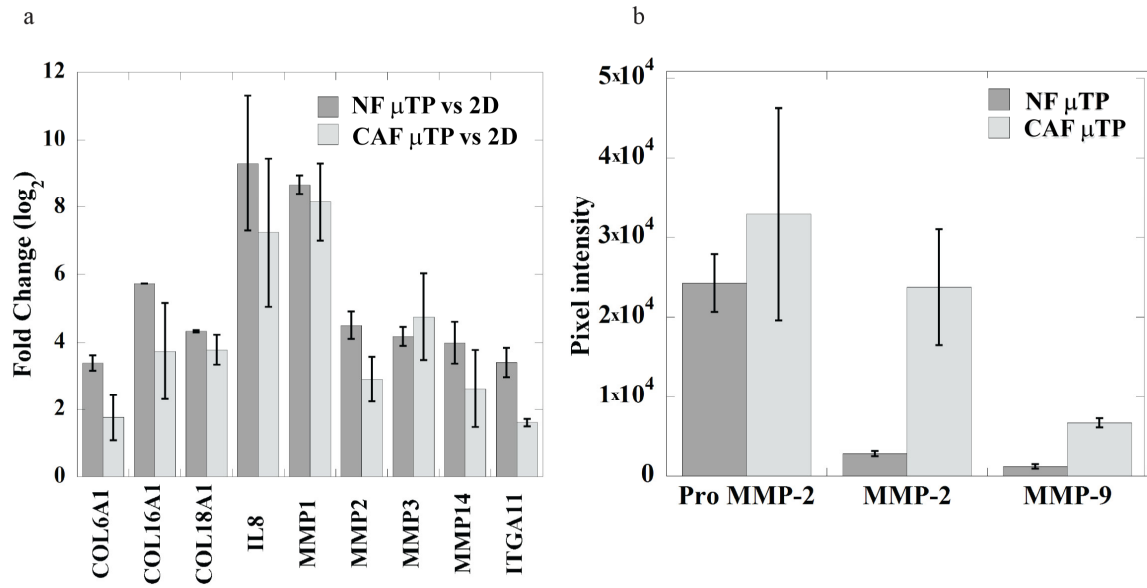


b

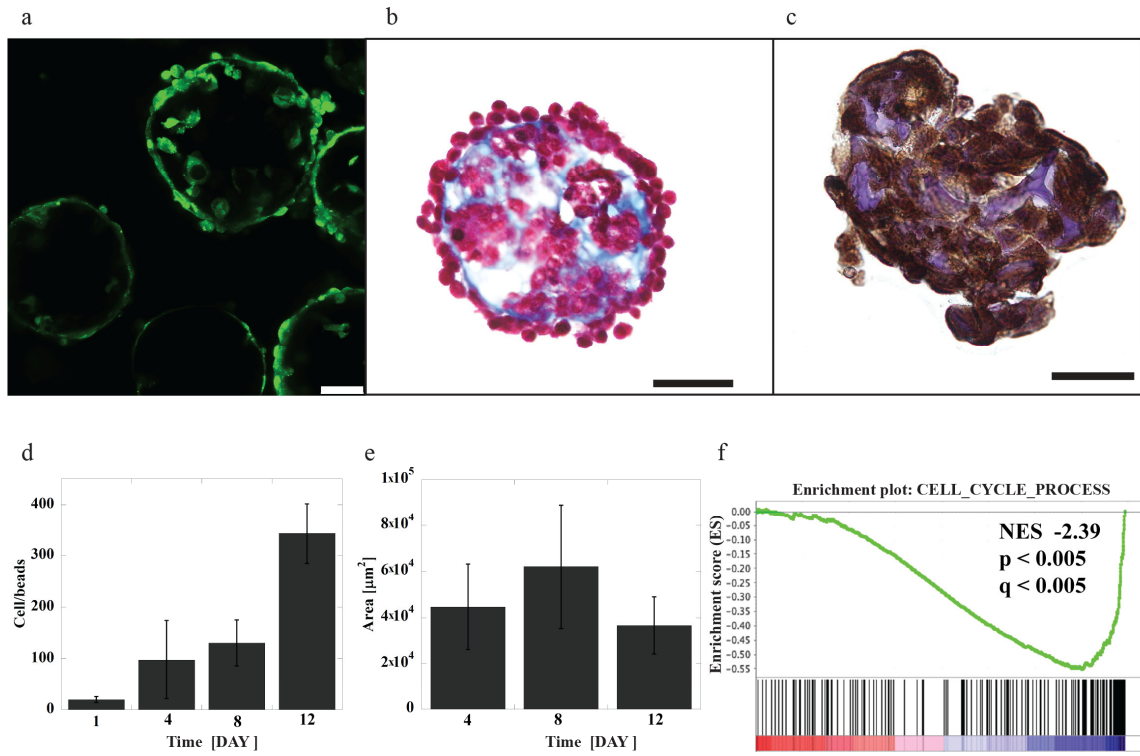


c

**NF  $\mu$ TP vs NF 2D**

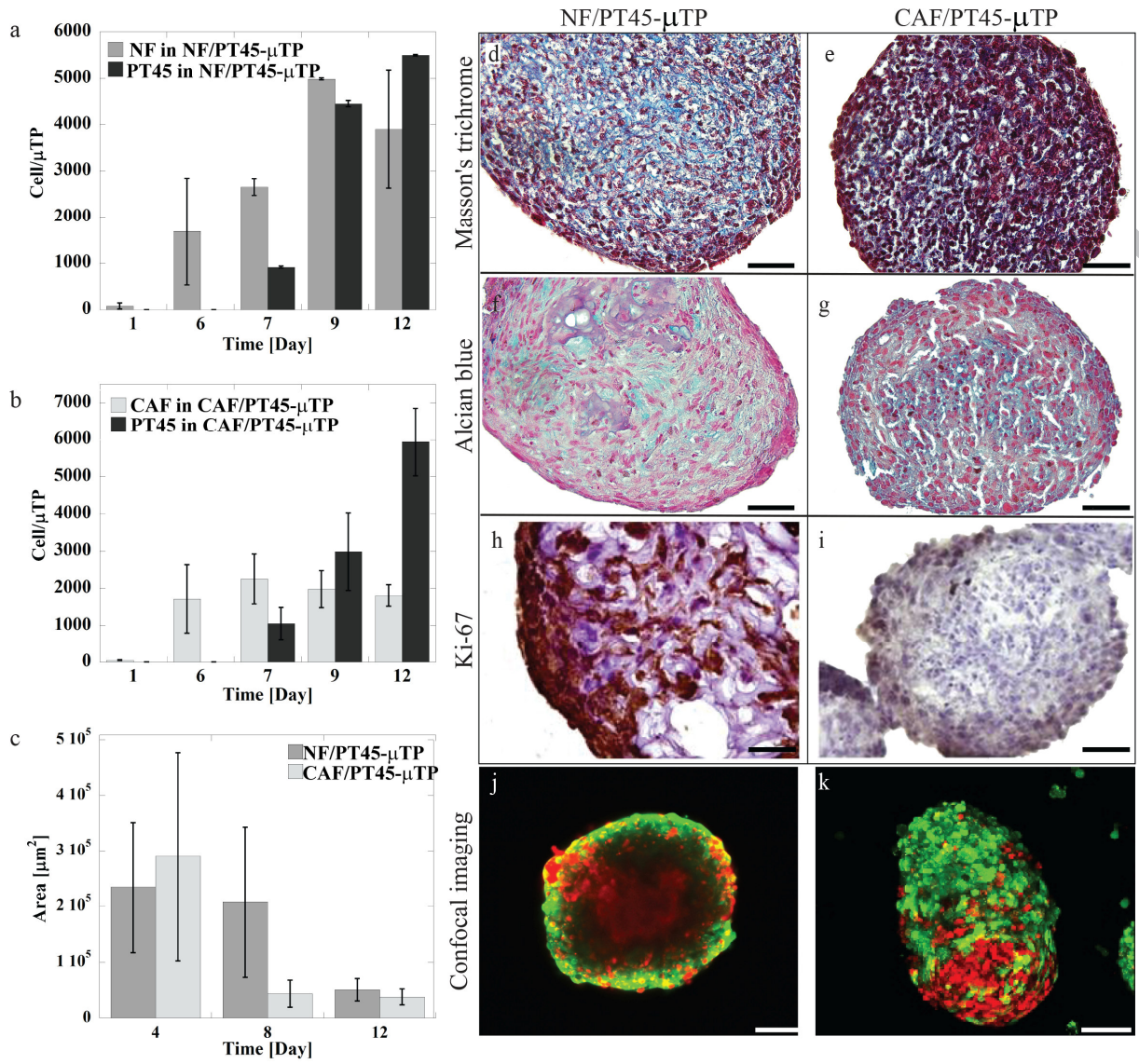


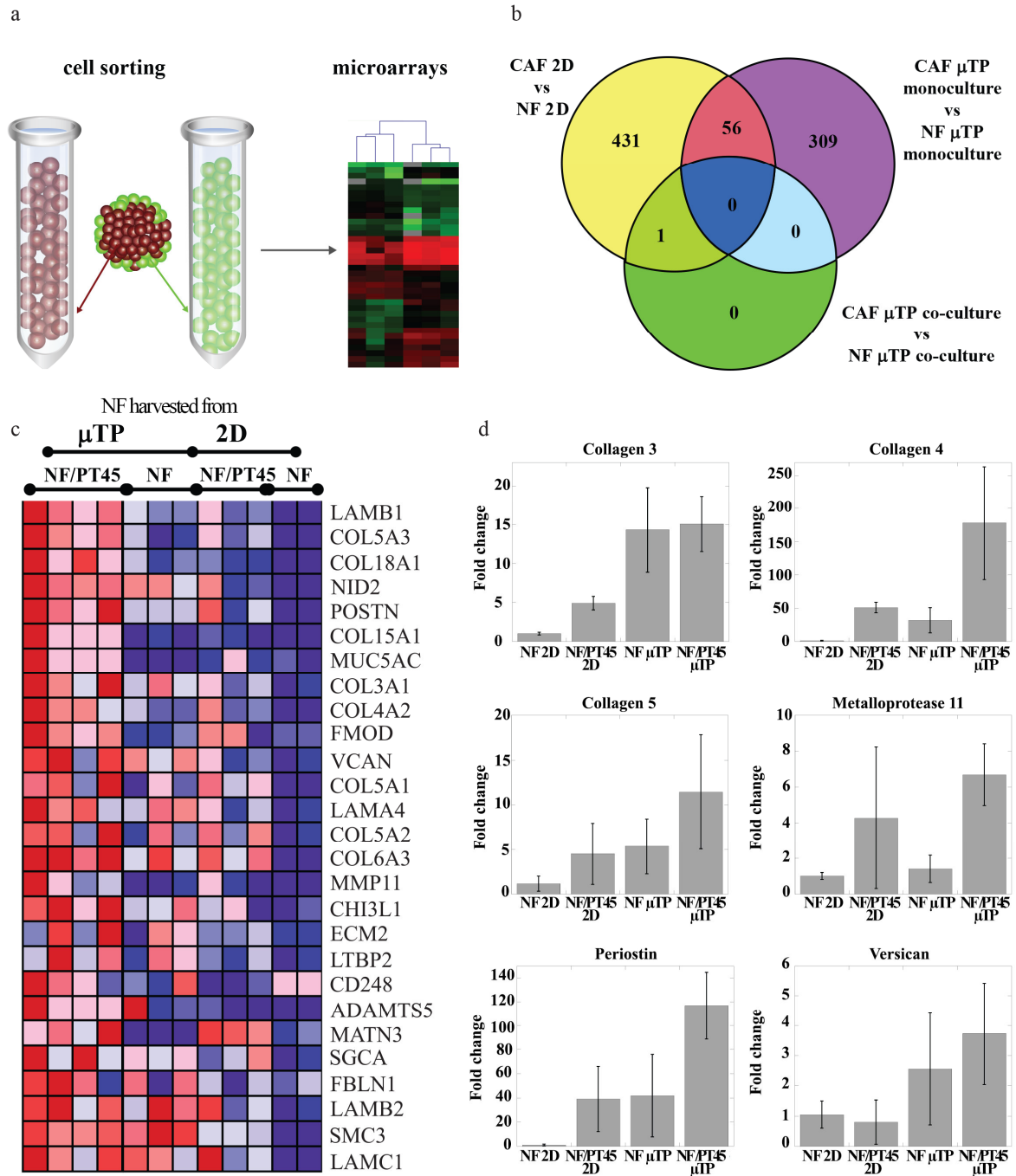
ACCEPTED MANUSCRIPT



ACCEPTED







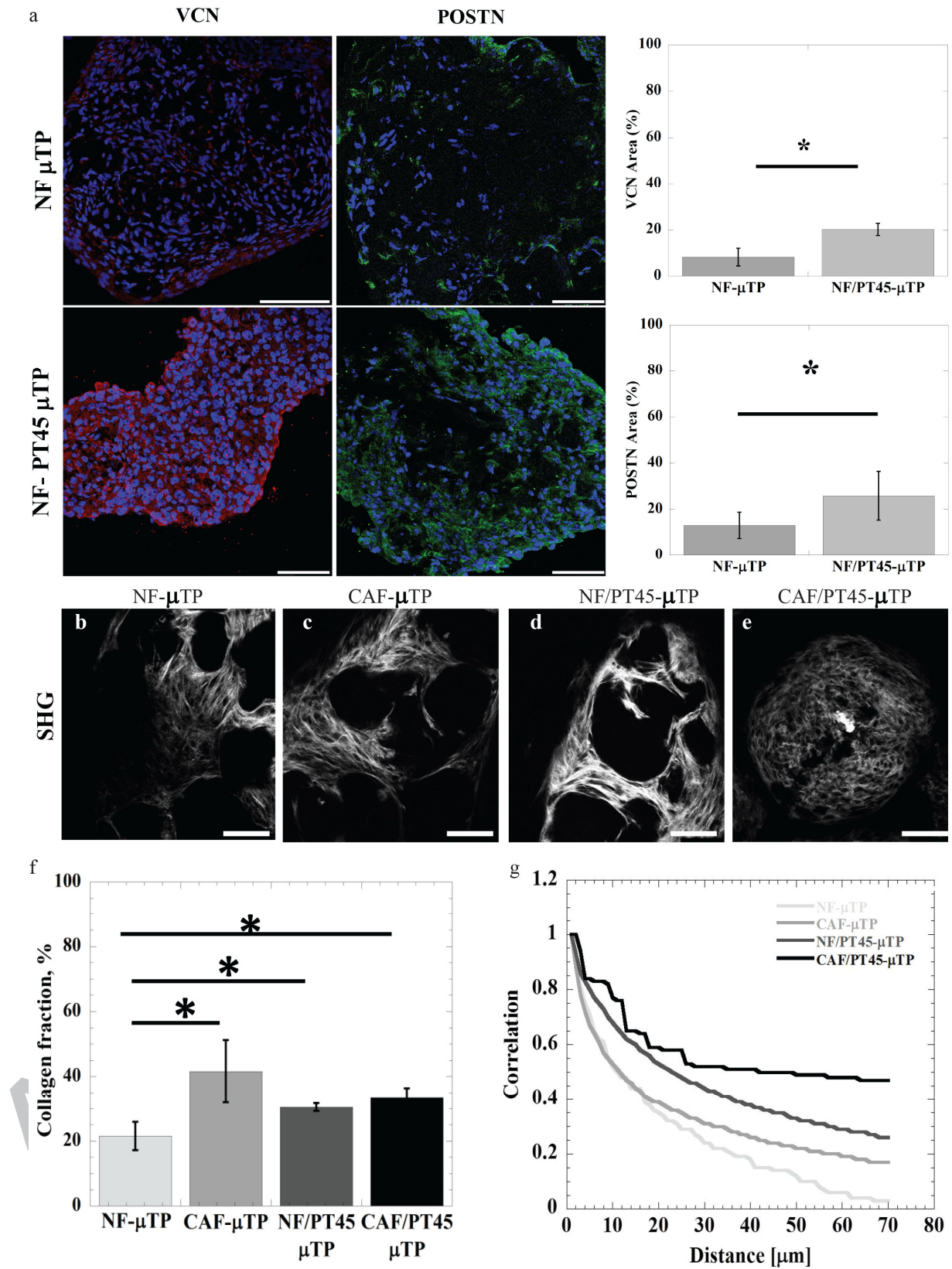




**Table 1. Molecular pathways found enriched by DAVID analysis of microarray data in NF**

| Up-Regulated GO terms                         | <b>-log10<br/>(pvalue)</b> | Down-regulated terms                                    | <b>-log10<br/>(pvalue)</b> |
|---|----------------------------|---|----------------------------|
| GO:0044421 extracellular region part          | 16,32                      | GO:0000279 M phase                                      | 13,33                      |
| GO:0031012 extracellular matrix               | 9,51                       | GO:0051301 cell division                                | 13,03                      |
| GO:0005578 proteinaceous extracellular matrix | 9,22                       | GO:0022403 cell cycle phase                             | 12,85                      |
| GO:0044420 extracellular matrix part          | 8,51                       | GO:0007049 cell cycle                                   | 12,68                      |
| GO:0005576 extracellular region               | 8,34                       | GO:0048285 organelle fission                            | 12,40                      |
| GO:0005615 extracellular space                | 7,58                       | GO:0000280 nuclear division                             | 12,33                      |
| GO:0009611 response to wounding               | 5,64                       | GO:0007067 mitosis                                      | 12,33                      |
| GO:0022610 biological adhesion                | 5,51                       | GO:0000087 M phase of mitotic cell cycle                | 12,16                      |
| GO:0007155 cell adhesion                      | 5,22                       | GO:0000278 mitotic cell cycle                           | 10,71                      |
| GO:0042127 regulation of cell proliferation   | 5,02                       | GO:0022402 cell cycle process                           | 10,67                      |
| GO:0005581 collagen                           | 4,68                       | GO:0043232 intracellular non-membrane-bounded organelle | 7,35                       |
| GO:0030198 extracellular matrix organization  | 4,47                       | GO:0043228 non-membrane-bounded organelle               | 7,35                       |
| GO:0042981 regulation of apoptosis            | 4,32                       | GO:0000775 chromosome, centromeric region               | 6,43                       |
| GO:0030334 regulation of cell migration       | 4,29                       | GO:0044427 chromosomal part                             | 5,81                       |

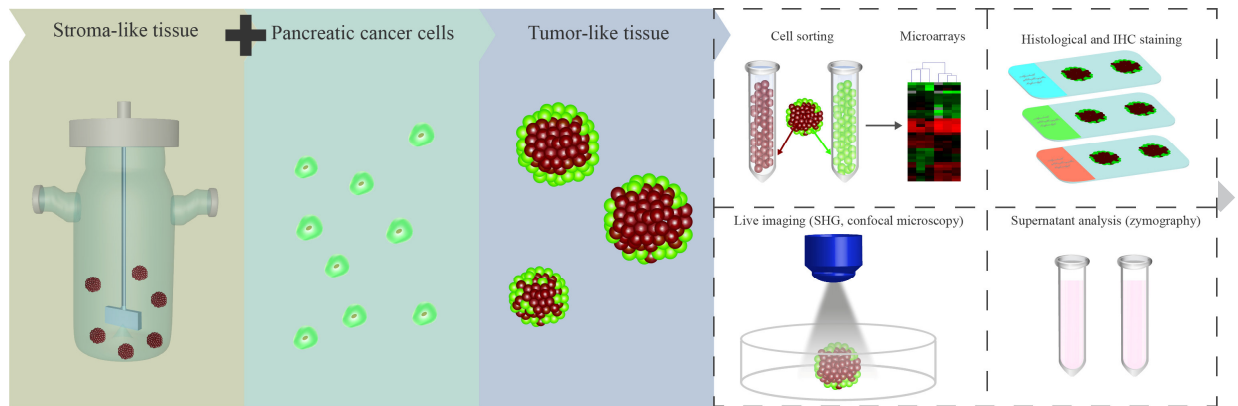
**Table 2. Molecular pathways found enriched by DAVID analysis of microarray data in PT45**

| <b>Up-Regulated gene family</b>   | <b>-log<sub>10</sub> (pvalue)</b> |
|---|-----------------------------------|
| GO:0005576 extracellular region   | 4,53                              |
| GO:0032393 MHC class I receptor activity  | 3,81                              |
| GO:0002474 antigen processing and presentation of peptide antigen via MHC class I | 3,14                              |
| GO:0042612 MHC class I protein complex  | 2,94                              |
| GO:0048002 antigen processing and presentation of peptide antigen                 | 2,28                              |
| <b>Down-regulated gene family</b>   | <b>-log<sub>10</sub> (pvalue)</b> |
| GO:0007049 cell cycle   | 4,21                              |
| GO:0022402 cell cycle process   | 3,82                              |
| GO:0022403 cell cycle phase   | 2,75                              |
| GO:0000279 M phase  | 2,49                              |
| GO:0006563 L-serine metabolic process   | 2,40                              |
| GO:0000278 mitotic cell cycle   | 2,17                              |
| GO:0009070 serine family amino acid biosynthetic process                          | 2,12                              |
| GO:0016053 organic acid biosynthetic process                                      | 1,99                              |
| GO:0046394 carboxylic acid biosynthetic process                                   | 1,99                              |
| GO:0016126 sterol biosynthetic process  | 1,96                              |
| GO:0006564 L-serine biosynthetic process  | 1,90                              |
| GO:0051301 cell division  | 1,75                              |
| GO:0000775 chromosome, centromeric region   | 1,71                              |
| GO:0000779 condensed chromosome, centromeric region                               | 1,70                              |

**Statement of significance**

Tumor microenvironment is extremely complex and its organization is due to the interaction between different kind of cells and the extracellular matrix. Tissue engineering could give the answer to the increasing need of 3D culture model that better recapitulate the tumor features at cellular and extracellular level. We aimed in this work at developing a microtissue tumor model by mean of seeding together cancer cells and fibroblasts on gelatin microsphere in order to monitor the crosstalk between the two cell populations and the endogenous extracellular matrix deposition. Results are of particular interest because of the need of heterotypic cancer model that can replicate the complexity of the tumor microenvironment and could be used as drug screening platform.

ACCEPTED MANUSCRIPT



ACCEPTED MANUSCRIPT